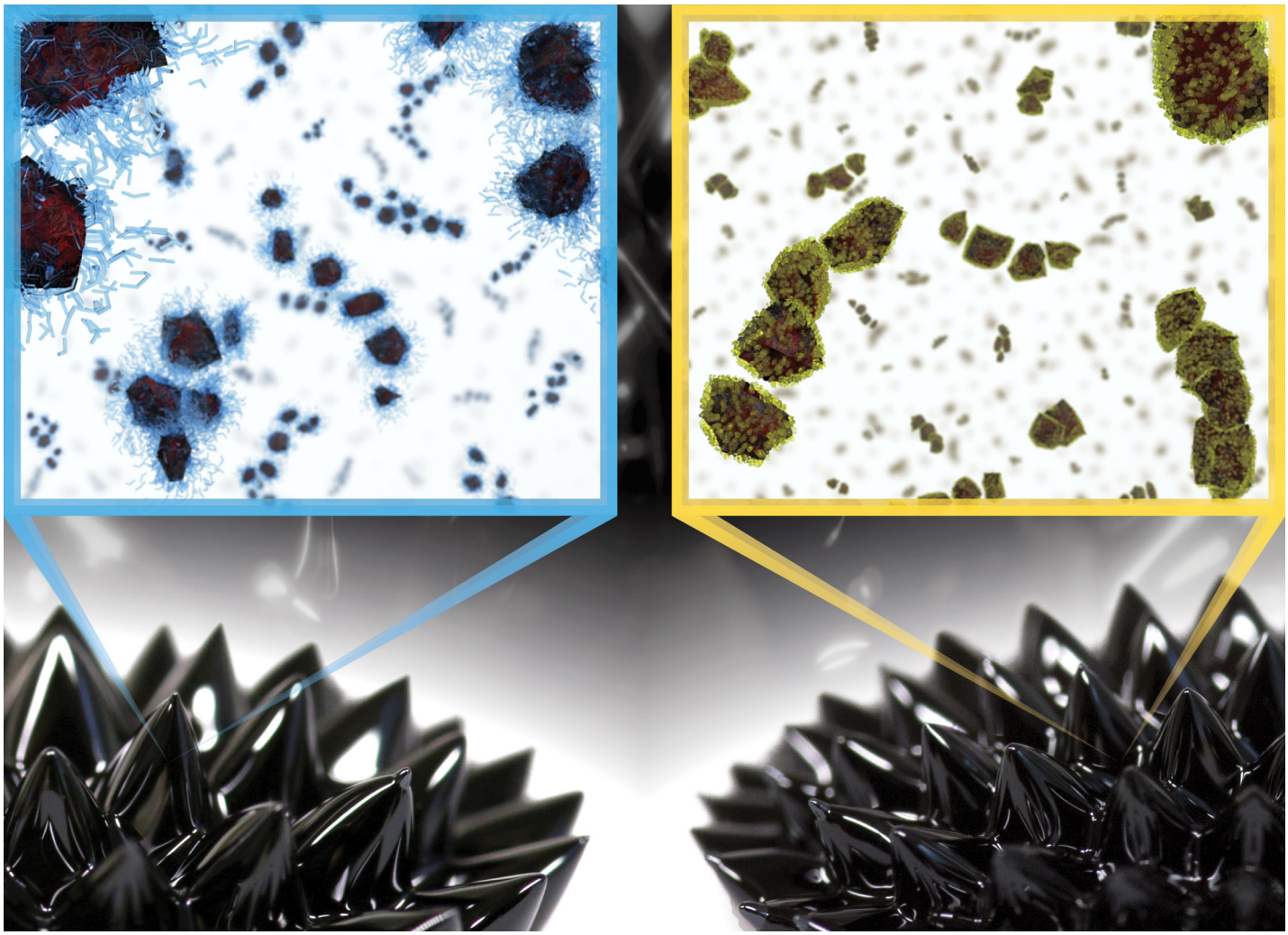

Highlighting cooperative research performed at the Laboratory of Magnetic Fluids – Romanian Academy, Timisoara Branch (Romania), Department of Applied Physics – Aalto University (Finland), Physics Department – Institute for Energy Technology (Norway), Helmholtz Zentrum Geesthacht – Centre for Materials and Coastal Research (Germany), National Institute for R&D of Isotopic and Molecular Technologies, Cluj-Napoca (Romania) and Department of Food Engineering – University of Szeged (Hungary).

High concentration aqueous magnetic fluids: structure, colloidal stability, magnetic and flow properties

Magnetic fluids, with the unique coexistence of magnetic and liquid properties, exhibit fascinating phenomena such as magnetic field induced pattern formation (shown in the bottom corners of the cover image). A wide range of advanced techniques were used to study two types of water based magnetic fluids with electro-steric (oleic acid, blue) and electrostatic (citric acid, green) nanoparticle stabilization, showing both similarities and important differences in their microscopic and macroscopic properties.

As featured in:

See K. D. Knudsen, L. Vékás *et al.*, *Soft Matter*, 2018, **14**, 6648.

ROYAL SOCIETY OF CHEMISTRY

rsc.li/soft-matter-journal

Registered charity number: 207890

Soft Matter

PAPER

View Article Online
View Journal | View Issue

Cite this: *Soft Matter*, 2018, **14**, 6648

High concentration aqueous magnetic fluids: structure, colloidal stability, magnetic and flow properties†

Corina Vasilescu, [ab] M. Latikka, [c] K. D. Knudsen, [*de] V. M. Garamus, [f] V. Socoliuc, [b] Rodica Turcu, [g] Etelka Tombácz, [h] Daniela Susan-Resiga, [bi] R. H. A. Ras [cj] and L. Vékás [*b]

This paper is an in-depth analysis devoted to two basic types of water based magnetic fluids (MFs), containing magnetite nanoparticles with electrostatic and with electro-steric stabilization, both obtained by chemical coprecipitation synthesis under atmospheric conditions. The two sets of magnetic fluid samples, one with citric acid (MF/CA) and the other with oleic acid (MF/OA) coated magnetic nanoparticles, respectively, achieved saturation magnetization values of 78.20 kA m^{-1} for the electrostatically and 48.73 kA m^{-1} for the electro-sterically stabilized aqueous ferrofluids which are among the highest reported to date. A comprehensive comparative analysis combining electron microscopy, X-ray photoelectron spectroscopy, attenuated total reflectance Fourier transform infrared spectroscopy, vibrating sample magnetometry, small-angle X-ray and neutron scattering, dynamic light scattering and magneto-rheometry revealed similarities and essential differences on the microscopic and macroscopic level between the two kinds of water-based ferrofluids. While the saturation magnetization values are quite different, the hydrodynamic volume fractions of the highest concentration MF/CA and MF/OA samples are practically the same, due to the significantly different thicknesses of the particles' coating layers. The results of volume fraction dependent structure analyses over a large concentration range by small-angle X-ray and neutron scattering, correlated with magneto-rheological investigations for the electrostatically stabilized MFs, demonstrate formation of short chains of magnetic nanoparticles which are relatively stable against coagulation with increasing concentration, while for MFs with electro-steric stabilization, magnetic field and shear rate dependent loosely bound structures are observed. These particle structures in MF/OA samples manifest themselves already at low volume fraction values, which can be attributed mainly to magnetic interactions of larger size particles, besides non-magnetic interactions mediated by excess surfactant.

Received 8th December 2017,
Accepted 30th June 2018

DOI: 10.1039/c7sm02417g

rsc.li/soft-matter-journal

[a] *Department of Applied Chemistry and Organic and Natural Compounds Engineering, Faculty of Industrial Chemistry and Environmental Engineering, Politehnica University Timisoara, Carol Telbisz 6, 300001 Timişoara, Romania*
[b] *Laboratory of Magnetic Fluids, Center for Fundamental and Advanced Technical Research (CFATR), Romanian Academy, Mihai Viteazul Str. 24, 300223 Timisoara, Romania. E-mail: vekas.ladislau@gmail.com*
[c] *Department of Applied Physics, School of Science, Aalto University, Puumiehenkuja 2, 02150 Espoo, Finland*
[d] *Physics Department, Institute for Energy Technology (IFE), 2027 Kjeller, Norway. E-mail: kenneth.knudsen@ife.no*
[e] *Department of Physics, Norwegian University of Science and Technology (NTNU), 7495 Trondheim, Norway*
[f] *Helmholtz-Zentrum Geesthacht, Centre for Materials and Coastal Research, Max-Planck-Str. 1, 21502 Geesthacht, Germany*
[g] *National Institute for Research and Development of Isotopic and Molecular Technologies (INCDTIM), Donat Str. 67-103, 400293 Cluj-Napoca, Romania*
[h] *Department of Food Engineering, Faculty of Engineering, University of Szeged, Moszkvai krt. 5-7, H-6725 Szeged, Hungary*
[i] *Faculty of Physics, West University of Timisoara, V. Parvan Bd. 4, 300223 Timisoara, Romania*
[j] *Department of Bioproducts and Biosystems, School of Chemical Engineering, Aalto University, Kemistintie 1, 02150 Espoo, Finland*

† Electronic supplementary information (ESI) available: Fig. S1. ATR-FTIR spectra measured from dried solutions of the electrostatically stabilized magnetic fluid, uncoated iron oxide nanoparticles and citric acid. The pH of the MF/CA sample was ~7 and that of the reference samples was adjusted to ~7. Fig. S2. ATR-FTIR spectra measured from dried solutions of the electro-sterically stabilized magnetic fluid, uncoated iron oxide nanoparticles and oleic acid. The pH of the MF/OA sample was ~9 and that of the reference samples was adjusted to ~9. See DOI: 10.1039/c7sm02417g

1. Introduction

To ensure long-term colloidal stability of magnetic fluids (MFs), the overall particle interaction potential should provide an energy barrier in order to keep particles apart and homogeneously distributed in the volume of the carrier liquid.[1] Attractive van der Waals and magnetic forces are ubiquitous and therefore must be balanced by Coulombic, steric or other interactions to control the colloidal stability of dispersed nanoparticle systems, even in intense and strongly non-uniform magnetic fields.[2–5] High saturation magnetization ferrofluids should have the magnetic particle volume fraction as large as possible and, at the same time, avoid aggregate formation. These requirements are hard to satisfy, especially in the case of water based magnetic fluids. Long-term colloidal stability of concentrated magnetic fluids is more challenging for aqueous than for organic carriers. The increase of the physical volume fraction necessary to attain high saturation magnetization involves a corresponding increase of the hydrodynamic volume fraction, however to different extents depending on the stabilization mechanism, electrostatic or electro-steric.[6] The advantage of electrostatically stabilized fluids is the reduction of the total suspended material at constant magnetic volume fraction compared with a surfactant stabilized fluid,[4] due to the much greater thickness of the steric stabilizing layer.

The surface charge has the main role in electrostatic stabilization of aqueous magnetic fluids,[7] consequently the pH and ionic strength of the dispersion medium strongly influence the stability of the ferrofluid.[3,8] Surface ions are produced from surface groups through acid–base reactions (surface iron atoms are bridged by OH, an amphoteric group) or by complexing agents (ligands) of some surface atoms (*e.g.* citrate ions bound to iron atoms).[9] The adsorption of complexing ligands leads to a shift of the IEP value (the isoelectric point, *i.e.*, the pH at which a colloidal particle carries no net electrical charge and so loses its electrostatic stabilization); using citrate ligands the coagulation range is shifted to pH < 4. The colloidal stability is ensured by a balance between magnetic, van der Waals, hard core repulsion and screened electrostatic interactions of particles,[10–12] as well as the osmotic pressure and ionic strength controlling the state of interaction of the dispersion. Exploring a very wide range of particle volume fraction values, 1–30%,[13–15] a critical volume fraction was determined expressing the freezing of the rotational dynamics of magnetic nanoparticles. The critical volume fraction strongly depends on the size of nanoparticles and the ionic strength of the dispersion.

Engineering applications, such as sink-float separators, stimulated the synthesis of relatively concentrated aqueous ferrofluids (saturation magnetization up to 38 kA m^{-1}) with surfactant double layer steric stabilization, a procedure introduced by Shimoiizaka and coworkers,[16] using sodium dodecylbenzene sulfonate, poly(oxyethylene)nonylphenylethers, and di(2-ethylhexyl) adipate, which adsorb as a second layer on the chemisorbed oleic acid first layer. Increased dilution stability of water based ferrofluids was achieved by steric stabilization with lauric acid as the particle surface coating agent.[17] Mostly motivated by biomedical and biotechnology applications,[18–21] the electrosteric stabilization of iron–oxide nanoparticles in an aqueous medium is widely applied, using various kinds of stabilizing bilayers, to produce stable water based magnetic fluids.[22–27] In the case of the fatty acids normally used as surfactants for forming double layers, the first layer is chemically bound on the particle surface (–COOH binds to the $Fe\equiv OH$ site), while the second layer forms *via* hydrophobic interaction of alkyl chains. This thick coating can effectively hinder the aggregation of magnetite particles due to the combined steric and electrostatic stabilization.[28,29] This procedure requires an excess of free surfactant in solution, which leads to the appearance of micelles that can affect negatively the stabilization of magnetic particles,[30,31] as it was evidenced earlier in the case of ferrofluids with organic carriers.[32] Unlike the charge stabilization of aqueous magnetic fluids, the stabilization in the above case is predominantly determined by steric factors due to the increase in the average distance between particles and the decrease in the dipole–dipole interaction energy that limits cluster formation.[33] The usually low iron oxide volume fraction (well below 10%) limits the saturation magnetization of water based magnetic fluids to approx. 100–200 G (8–16 kA m^{-1}), mainly because of the particle aggregation tendency at higher concentrations[5] and especially in biorelevant aqueous media.[34] Progress has been related to use of triblock polymers synthesized with controlled concentrations of carboxylic acid binding groups in central polyurethane segments and poly(ethylene oxide) end blocks, which were successfully used as hydrophilic steric stabilizers for Fe_3O_4 particles with a mean size of 8.8 nm to obtain water based magnetite ferrofluids;[35] the highest concentration of dispersed surface coated magnetite nanoparticles attained 45 wt%. By stabilizing 7 nm mean size γ-Fe_2O_3 nanoparticles with a very thin (approx. 1 nm) layer of a short, water soluble diblock copolymer of acrylic acid and acrylamide, high concentration (up to 65 wt%) colloidally stable magnetic fluids resulted[36] with 2 M NaCl solution as the carrier leading to a saturation magnetization of approx. 42.6 kA m^{-1}.

Colloidal stability issues, involving nanoparticle size and magnetic moment, dipolar interactions, excess surfactant and agglomerate formation, have strongly influenced the highest values of saturation magnetization achieved. Compared to magnetic fluids with organic carriers, in aqueous magnetic fluids significantly stronger interparticle interactions result in larger and more compact clusters with higher fractal dimensions.[37] Small-angle scattering techniques using neutron beams (SANS) or X-rays (SAXS) are sensitive to the onset and development of structuring in magnetic fluids and offer reliable information on colloidal stability[5,38–41] up to the highest values of particle volume fraction. Rheological and magnetorheological investigations in the case of water based magnetic fluids refer mostly to bioferrofluids[42,43] or to biopolymer based magnetoresponsive particle suspensions.[44] While the magnetic nanoparticle content of these magnetoresponsive colloidal systems is limited to 1–2%, the magnetic interaction parameter is well above 1 for multi-core magnetic particles explaining the observed high magnetoviscous effect.[43] The applications in biotechnology and biomedicine of

magnetic nanoparticle dispersions stabilized by electrostatic repulsion or surfactant bilayers are governed by their sensitivity to conditions such as pH and ionic strength and/or protein adsorption in the biological environment. This is especially important when these particles are to be administered into a living organism and the colloidal dispersions therefore need to be very stable at both neutral pH and high ionic strength. Considering the good colloidal behaviour of citric acid (CA) stabilized ferrofluids at different pH and electrolyte compositions, as well as their non-toxicity, CA coating of magnetic nanoparticles (MNPs) could be envisaged as a good strategy to increase the stability of MNPs in environmental applications,[45] as well as in preparation of high magnetization nanocomposites to be used as contrast agents and drug targeting vehicles[46,47] which involves the encapsulation of initially individually stabilized iron oxide nanoparticles up to high volume fractions. Oleic acid (OA) covered magnetite nanoparticles as-prepared or encapsulated in magnetoresponsive nanocomposites[48] can represent optimal candidates to be used in magnetic bio-separation,[24,49] environmental sensing, imaging and remediation[50] and as contrast agents for imaging the brain, since OA bilayer coated MNPs bearing a protein corona more enriched in lipoproteins and albumin than complement and immunoglobulin proteins might better escape the immune system.[51] OA bilayer structures were applied also to facilitate the transfer of iron oxide nanoparticles (IONPs), obtained by thermal decomposition of iron carboxylate salts at high temperature, from hexane to water.[50] Beside biotechnology and biomedical applications, the aqueous ferrofluids with iron oxide nanoparticles characterized by high magnetization at saturation and long-term colloidal stability are of particular interest for magneto-gravimetric separators[16,17,52–55] and require large-scale cost-effective manufacturing, favouring ferrofluid synthesis by chemical coprecipitation.[56]

In this paper two types of highly concentrated water based magnetic fluids, one with electrostatic and the other with electro-steric stabilization, were prepared and investigated. In both cases the magnetite nanoparticles were synthesized by chemical coprecipitation, but the samples are significantly different concerning the particle hydrodynamic volume fraction and the highest saturation magnetization achieved, depending on the stabilization procedure applied. Manifold advanced techniques, such as TEM, DLS, SAXS, SANS, XPS, ATR-FTIR, VSM and magneto-rheometry, were applied to probe and evaluate the differences and similarities concerning the structure and behaviour of the two kinds of water based magnetic fluid samples. To our best knowledge these are among the highest magnetization water based magnetic fluids synthesized and comparatively analysed.

2. Materials and methods

2.1. Materials

The materials used to obtain the citrate sample were: $FeCl_3 \cdot 6H_2O$, $\geq$99%; $FeCl_2 \cdot 4H_2O$, $\geq$99.0%; NH_4OH, 28.0–30.0%; citric acid monohydrate, $\geq$99.5%; and acetone, $\geq$99.8%. All primary materials were purchased from Sigma-Aldrich and used as received.

The materials used in the case of the oleic acid sample were: $FeCl_3$ and $FeSO_4$, purchased from Merck; and oleic acid (technical grade, 90%), purchased from Sigma-Aldrich. Ammonium hydroxide NH_4OH 25% was purchased from a local manufacturer.

2.2. Synthesis of water based magnetic fluids with electrostatic stabilization

A successful synthesis route for magnetite nanoparticles with electrostatic stabilization in a water carrier, only slightly different from Massart's procedure,[7] was described in ref. 57–59. Iron oxide nanoparticles were synthesized by coprecipitation of an aqueous mixture of $FeCl_3$ and $FeCl_2$ salts and stabilized with citric acid near pH 7.[2,57] 43.3 g of $FeCl_3$ and 15.9 g of $FeCl_2$ were dissolved in 1440 g of Milli-Q water. 160 mL of NH_4OH was added to precipitate the particles in ambient conditions under vigorous stirring, with the pH reaching up to 11. 50.4 g of citric acid monohydrate was added after 5 minutes of stirring to stabilize the nanoparticles. Stirring was continued for an additional 5 minutes after which the supernatant was removed using magnetic decantation. 200 mL of Milli-Q water and 8.4 g of citric acid monohydrate were added and the suspension was stirred for an additional 5 minutes. The suspension was washed several times with acetone and Milli-Q water using magnetic decantation, and after that excess water was evaporated at room temperature to achieve a nanoparticle concentration of 20 vol%. A series of samples from 0.5 vol% to 20 vol% were prepared by diluting the concentrated ferrofluid with Milli-Q water.

2.3. Synthesis of water based magnetic fluids with electro-steric stabilization

Iron oxide nanoparticles were synthesized by chemical coprecipitation from $FeCl_3$ and $FeSO_4$ salt solutions by addition of a base and subsequently coated with oleic acid at 80 °C according to the basic procedure outlined in ref. 28. In a typical synthesis, 60 grams of $FeSO_4$ was dissolved in 200 mL distilled water and mixed with 130 mL of a $FeCl_3$ solution of appropriate concentration. The Fe^{3+}/Fe^{2+} ratio used was adjusted to 1.7 since the preparation was done in atmospheric conditions in the presence of oxygen. This mixture was heated to 80 °C under vigorous mechanical stirring and precipitated with the use of a concentrated ammonia solution, with the pH value of the reaction medium approaching 11. Immediately after the formation of a black precipitate, 25 mL of oleic acid was added and the stirring was continued for 15 minutes.

The obtained precipitate was washed several times with distilled water to remove residual salts and then dispersed in water with the addition of ammonia at pH around 8.5.

After repeated purification steps the above laboratory scale synthesis procedure leads to approx. 50 g OA coated hydrophilic magnetite NPs. Dilution series of the two ferrofluids were prepared (Tables 1 and 2) since their concentration dependent properties are of importance. The solid matter contents of ferrofluids range from 0.5% to 20% volume fraction for the electrostatically stabilized particles (MF/CA) and from 0.5% to 14% for the electro-sterically stabilized ones (MF/OA). In both cases the pH varies with dilution, but not by more than approx. 1.2 units. The citrated

Table 1 Water based citrated ferrofluid samples with electrostatic stabilization

Sample code	Stabilizing ligand (monolayer)	Solid volume fraction [%]	Density [g cm^{-3}]
MF/CA1	Citric acid	0.50	1.019
MF/CA2	Citric acid	2.27	1.093
MF/CA3	Citric acid	4.05	1.167
MF/CA4	Citric acid	5.82	1.241
MF/CA5	Citric acid	7.59	1.315
MF/CA6	Citric acid	9.36	1.389
MF/CA7	Citric acid	11.14	1.463
MF/CA8	Citric acid	12.91	1.537
MF/CA9	Citric acid	14.68	1.611
MF/CA10	Citric acid	16.45	1.685
MF/CA11	Citric acid	18.23	1.759
MF/CA12	Citric acid	19.99	1.833

Table 2 Water based surfacted ferrofluid samples with electro-steric stabilization

Sample code	Surfactant (double layer)	Solid volume fraction [%]	Density [g cm^{-3}]
MF/OA1	Oleic acid	0.50	1.021
MF/OA2	Oleic acid	1.00	1.042
MF/OA3	Oleic acid	2.00	1.084
MF/OA4	Oleic acid	4.00	1.168
MF/OA5	Oleic acid	6.00	1.252
MF/OA6	Oleic acid	8.00	1.337
MF/OA7	Oleic acid	10.00	1.180
MF/OA8	Oleic acid	12.00	1.504
MF/OA9	Oleic acid	14.00	1.588

Fig. 1 Normal field instability "spikes" of the water based magnetic fluid samples on a permanent magnet (NdFeB): (a) with electrostatic stabilization; and (b) similar with electro-steric stabilization.

samples have a pH between 6.4 and 7.1, while the oleic acid samples present pH values between 8.0 and 9.2. Small quantities of the most concentrated samples of both types of water based magnetic fluids were placed on NdFeB permanent magnets to illustrate their strong magnetic response (Fig. 1).

It is worth mentioning that it is possible to synthesize both types of nanoparticles under the same conditions by using the so-called post-coating method where chemically adsorbing compounds like CA or OA are adsorbed on purified naked iron oxide NPs obtained in a single batch, as we have done in several cases before.[34,51,60,61] The drawback of this synthesis approach is that only low concentration samples can be prepared, while our goal in this work was to prepare and characterize highly concentrated magnetic fluids.

2.4. Characterization methods

The solid (physical), hydrodynamic and magnetic size distributions were studied using transmission electron microscopy (TEM), dynamic light scattering (DLS) and magnetogranulometry, respectively. Different characterization techniques, such as X-ray photoelectron spectroscopy (XPS), zeta potential (NanoZS), Dynamic Light Scattering (DLS), Small-Angle X-ray Scattering (SAXS), Small-Angle Neutron Scattering (SANS) and magnetorheometry were used to evaluate particle surface properties, surfactant adsorption, colloidal stability at different pH and particle volume fraction values, as well as cluster formation and flow properties.

2.4.1. TEM. Transmission electron micrographs of the nanoparticles were recorded with FEI Tecnai 12 Bio Twin and STEM Hitachi HD-2700 transmission electron microscopes. The TEM images were used to determine the statistics of the diameters of the iron oxide region of the nanoparticles using ImageJ.[62]

2.4.2. Dynamic light scattering. The mean hydrodynamic diameter of the iron oxide particles was determined at 25 ± 0.1 °C by dynamic light scattering (DLS), using the Nano ZS device from Malvern (UK), operating in backscattering mode at an angle of 173°. The concentration of the dispersions was set to give an optimal intensity of ~105 counts per second. The diluted samples were homogenized in an ultrasonic bath for 10 seconds prior to the measurements, after which 50 seconds relaxation was allowed. First the size, then the zeta potential, was measured in a disposable zeta cell (DTS 1070). The Smoluchowski equation was applied to convert electrophoretic mobility to an electrokinetic potential value. The accuracy of the zeta potential measurements is ± 5 mV. Cumulant analysis was used to evaluate correlation functions and to calculate *Z*-average hydrodynamic sizes. In the case of unstable, coagulating systems only the given kinetic stage can be compared, since the measurable hydrodynamic size increases in time.

2.4.3. Vibrating sample magnetometry. Magnetogranulometry. The full magnetization curves, including the initial susceptibility and saturation magnetization of aqueous ferrofluids, were determined using a vibrating sample magnetometer, VSM 880 – ADE Technologies, USA, at room temperature, in the field range 0 kA m^{-1} to 950 kA m^{-1}.

The temperature dependence of the magnetization at low field (0.1 T) under zero-field cooling (ZFC) and field-cooling (FC) conditions in the range 4–300 K was determined using a Cryogenic vibrating sample magnetometer.

The magnetization data were used for magnetogranulometry analysis[63] which consists of determination of the nanoparticle concentration and magnetic diameter distribution from non-linear regression of the experimental data with the magnetization model $M(H)$ for dense ferrofluids developed by Ivanov and coworkers:[64]

$$\begin{aligned} M(H) &= M_{\mathrm{L}}(H_{\mathrm{e}}) \\ &= n\int_{D_{\mathrm{m}}=0}^{\infty} m(D_{\mathrm{m}})\cdot f(D_{\mathrm{m}})\cdot L\left(\frac{\mu_0 m(D_{\mathrm{m}})H_{\mathrm{e}}(H)}{kT}\right)\cdot \mathrm{d}D_{\mathrm{m}} \\ H_{\mathrm{e}}(H) &= H + \frac{M_{\mathrm{L}}(H)}{3}\cdot\left(1+\frac{1}{48}\cdot\frac{\mathrm{d}M_{\mathrm{L}}(H)}{\mathrm{d}H}\right) \qquad (1) \\ f(D_{\mathrm{m}}) &= \frac{1}{D_{\mathrm{m}}\sigma\sqrt{2\pi}}\cdot \mathrm{e}^{-\frac{(\ln(D_{\mathrm{m}}/D_0))^2}{2\sigma^2}} \end{aligned}$$

where $H_e(H)$ is the effective field, D_m is the magnetic diameter, n is the nanoparticle concentration, $m(D_m) = m_s\pi(D_m)^3/6$ is the magnetic moment of the particle, L is the Langevin function $L(x) = \coth(x) - 1/x$, μ_0 is the magnetic permeability of vacuum, m_s is the saturation magnetization of magnetite, k is Boltzmann's constant and T is the temperature. $f(D)$ is the log-normal probability distribution function of the magnetic diameter with a D_0 median and a σ standard deviation of the diameter natural logarithm. The nonlinear regression of the magnetization curve with the model in eqn (1) provides numerical values for n, D_0 and σ.

2.4.4. Surface spectroscopy

XPS. The chemical composition (atomic concentrations) and the chemical state of the atoms at the surface of the magnetic nanoparticle the dried ferrofluid sample Fe_3O_4/OA9 or Fe_3O_4/CA12 were determined by X-ray Photoelectron Spectroscopy (XPS). The spectra were recorded using a SPECS spectrometer equipped with a dual-anode X-ray source Al/Mg, a PHOIBOS 150 2D CCD hemispherical energy analyzer and a multi-channeltron detector with a vacuum maintained at 1×10^{-9} Torr. The $Al_{K\alpha}$ X-ray source (1486.6 eV) operated at 200 W was used for the XPS investigations. The XPS survey spectra were recorded at 30 eV pass energy and 0.5 eV per step. The high-resolution spectra for individual elements (Fe, C, O) were recorded by accumulating 10 scans at 30 eV pass energy and 0.1 eV per step. The samples were dried on indium foil to allow the XPS measurements. The sample surface was cleaned by argon ion bombardment (300 V). Data analysis and curve fitting was performed using CasaXPS software with Gaussian–Lorentzian product functions.

ATR-FTIR. The magnetic fluids were also characterized using attenuated total reflectance Fourier transform infrared spectroscopy (ATR-FTIR). The spectra were recorded with a Unicam Mattson 3000 spectrometer and a PIKE Technologies GladiATR ATR accessory, using 4 cm^{-1} resolution and 32 scans per measurement. Measurements were performed by letting a droplet of sample solution dry on the diamond of the ATR accessory and measuring the spectrum of a dry sample in the wavenumber range 400–4000 cm^{-1} in absorbance mode. The background spectrum was recorded before measuring the samples and subtracted from the sample spectra.

2.4.5. SAXS. Small-angle X-ray scattering data were collected at the P12 BioSAXS beamline (PETRA 3, EMBL/DESY, Hamburg, Germany). A beam of size 0.1×0.2 mm^2 and photon energy 18.44 keV was applied. Calibration of the q-range was done using the diffraction pattern of silver behenate. The sample–detector distance was 4 m and the range for the scattering vector was 0.005–0.65 $Å^{-1}$. Data were normalized to the intensity of the transmitted beam. 20 μL of solutions of samples and buffer (H_2O) were put in glass capillaries of 1 mm diameter and placed on a Linkam Heating stage HFSX 350 (Surrey, UK) for temperature control ($T = 20 \pm 0.1$ °C). A single measurement (1 second) consisted of accumulation of 20 frames, each of 0.05 seconds. Possible radiation damage effects were checked by comparison with the reference (typically the first exposure) and automatically integrated and subtracted with a standard acquisition program.[65]

2.4.6. SANS. The small-angle neutron scattering experiments were carried out at the SANS installation at the JEEP-II reactor at Kjeller, Norway. The wavelength was set with a velocity selector (Dornier), using a resolution ($\Delta\lambda/\lambda$) of 10%. The beam divergence was set by an input collimator (18.4 or 8.0 mm diameter) located 2.3 m from the sample, together with a circular 7 mm aperture located close to the sample which defined the beam cross section. The detector was a 59 cm active diameter, 3He-filled RISØ type, mounted on rails inside the evacuated detector chamber. The sample–detector distance was varied between 1.0 and 3.4 m, and the wavelengths used were 5.1 and 10.2 Å. The resulting q-range for the experiment was 0.006–0.3 $Å^{-1}$. The solutions were put in 1 mm Starna quartz cuvettes. The cells were placed onto a copper-base for good thermal contact and mounted onto the sample stage in the sample chamber. Standard reductions of the scattering data, including transmission corrections, were conducted by incorporating data collected from the empty cell, and the blocked-beam background, according to the formula given in eqn (2):

$$I_S^{cor} = \left(\frac{I_S}{M_S} - \frac{I_{BG}}{M_{BG}}\right) - \frac{T_S}{T_{EC}}\left(\frac{I_{EC}}{M_{EC}} - \frac{I_{BG}}{M_{BG}}\right) \quad (2)$$

Here I_S is the measured scattered intensity for the sample inside the quartz cell, I_{BG} is the intensity of the blocked-beam background, and I_{EC} is the intensity of the empty quartz cell. T_S and T_{EC} are the transmission values (<1) of the sample and of the empty cell, respectively. All the measurements were normalized to the beam monitor counts (M_i) to compensate for possible variations in the incoming beam flux. Finally, all data were transformed to an absolute scale (coherent differential cross section ($d\Sigma/d\Omega$)), making use of the intensity value registered in open beam measurements (no sample or cell), with a calibrated attenuator (Cd-mask with holes) in the beam,[66] before averaging radially to produce an $I(q)$ *vs.* q pattern.

2.4.7. Modelling of SAXS & SANS data. To account for possible deviations from spherical entities, the scattered intensity $I(q)$ was modelled as coming from a population of ellipsoids of rotation or cylindrical particles. $I(q)$ can be described in a decoupling approximation (no correlation between the size/orientation and position of particles) by the following equation:[67]

$$I(q) = I(0)P(q)S'(q) + B \quad (3)$$

where

$$P(q) = \langle|F(q)|^2\rangle \quad (4)$$

$$S'(q) = 1 + \beta(q)\cdot[S(q) - 1] \quad (5)$$

$$\beta(q) = |\langle F(q)\rangle|^2/\langle|F(q)|^2\rangle \quad (6)$$

The inner brackets $\langle\rangle$ in eqn (4) and (6) represent an average weighted by the distribution of particle sizes and/or orientations, $I(0)$ is the scattering at zero angle (proportional to the concentration of particles, contrast, and particle volume), $P(q)$ is the form factor, $F(q)$ is the amplitude of the form factor, $S(q)$ is the structure factor, and $S'(q)$ is the effective structure factor modified by the anisotropy and polydispersity of particles.

In the case of a core shell ellipsoid of rotation of semiaxes a, a and b, $F(q)$ is expressed as:

$$F(q) = 3(\rho_{\text{core}} - \rho_{\text{solvent}})V_{\text{core}}\frac{\sin(qR) - qR\cos(qR)}{(qR)^3} + 3(\rho_{\text{shell}} - \rho_{\text{solvent}})V_{\text{shell}} \times \frac{\sin(q(R+T)) - q(R+T)\cos(q(R+T))}{(q(R+T))^3} \quad (7)$$

where $R = [b^2{\cdot}\sin^2\alpha + a^2{\cdot}\cos^2\alpha]^{1/2}$ and α is the angle between the axis of the ellipsoid a and the scattering vector q, and T is the thickness of the shell. A log normal distribution of b was used in the analysis.

In the case of core–shell cylinders, these expressions are slightly modified:

$$F(q) = 2(\rho_{\text{core}} - \rho_{\text{solvent}})V_{\text{core}}\frac{\sin(qL/2\cos\beta)2J_1(qR\sin\beta)}{(qL/2\cos\beta)(qR\sin\beta)} + 2(\rho_{\text{shell}} - \rho_{\text{solvent}})V_{\text{shell}} \times \frac{\sin(q(L+T)/2\cos\beta)2J_1(q(R+T)\sin\beta)}{(q(L+T)/2\cos\beta)(q(R+T)\sin\beta)} \quad (8)$$

where L is the length of the cylinder core, R is the radius of the cylinder core, J_1 is the first-order Bessel function, and β is the angle between the q-vector and the axis of the cylinder.

Two kinds of structure factors were used in the analysis: (i) the excluded volume interaction calculated with the Percus–Yevick approximation for the closure relation,[68] which requires as input parameters the hard sphere volume fraction and the effective hard sphere radius. The detailed expression for the function can be found in ref. 69. (ii) The screened Coulomb potential in the rescaled mean spherical approximation (RMSA) in the Penfold and Hayter form.[70,71] The $S(q)$ model requires as input parameters the temperature, the dielectric constant of the medium, the added salt concentration, and the volume fraction.

2.4.8. Magnetorheology. Rotational rheometer with a MR cell. The measurements of the flow properties of ferrofluids were performed using a PHYSICA MCR 300 (Anton Paar, Germany) equipped with a magnetorheological cell (MRD 170/1T-SN80730989). The MR cell has parallel plates of 20 mm diameter, with the gap being fixed at h = 0.2 mm. All the measurements were done at 20 °C. The magnetic flux density was determined using a Hall probe located as described in ref. 72 and 73 to ensure on-line measurement of the magnetic induction in the MR cell gap.

3. Results and discussion

3.1. Particle morphology and sizes: transmission electron microscopy

In Fig. 2 the TEM images and nanoparticle diameter histograms for the MF/CA and MF/OA samples are presented. The nanoparticles in both ferrofluids show irregular shapes which is typical for chemical coprecipitation synthesis. Table 3 presents the mean, standard deviation and skewness of the nanoparticle diameter, calculated based on measured sizes of more than 1000 particles for each ferrofluid sample. All distributions show positive skewness, in agreement with the log-normal distribution calculated from first principles by Cogoni and coworkers.[74,75] The MF/CA ferrofluid has particles of smaller average size than the MF/OA ferrofluid due to larger populations of small diameter nanoparticles (1–4 nm). Fig. 2e shows the normalized volume distributions of magnetic nanoparticles in the MF/CA and MF/OA samples. Large nanoparticles are in excess in the MF/OA ferrofluid, while small nanoparticles are in excess in the MF/CA ferrofluid. This makes the MF/OA ferrofluid more susceptible to magnetically driven structuring.

3.2. Magnetization curves and magnetogranulometry

We considered the highest concentrations of both the electrostatically and the electro-sterically stabilized ferrofluid samples, *i.e.* MF/CA12 and MF/OA9 (*cf.* Tables 1 and 2) to investigate in detail the magnetization properties of the two aqueous colloidal systems.

The temperature dependence of the magnetization of the ferrofluid samples in ZFC and FC regimes (Fig. 3a) show a typical superparamagnetic behaviour. The ZFC curves exhibit a broad peak, indicating a transition from the magnetically blocked state at low temperatures to a superparamagnetic state at high temperatures. The blocking temperatures for magnetic nanoparticles depend on the size, size distribution, surface state and interparticle interactions,[76] the broad peak reflecting the relatively wide size range of magnetic nanoparticles typical for synthesis by chemical coprecipitation. From a qualitative examination of Fig. 3a one can conclude that the maximum of the ZFC curve, which could be assigned to the blocking temperature, is higher for the oleic acid ferrofluid (MF/OA) than for the citrate ferrofluid (MF/CA). This result is in agreement with the nanoparticles' physical size and magnetic size determined from TEM and magnetogranulometry, respectively. The broadness of the ZFC curve indicates the existence of dipolar interactions between nanoparticles in both types of ferrofluid.

The magnetization curves of the citric acid and oleic acid stabilized water based magnetic fluid samples are presented in Fig. 3b. The initial susceptibility of the samples was 3.07 for MF/CA12 and 3.68 for MF/OA9 (Table 4). The saturation magnetization of the samples was determined using Chantrell's method,[77] *i.e.* from the linear fit of $M(1/H)$ data at high fields. The saturation magnetizations are 78.20 kA m^{-1} for the MF/CA12 sample and 48.73 kA m^{-1} for the MF/OA9 sample (Table 4). The non-dimensional magnetization curves, *i.e.* the magnetization scaled to the saturation magnetization, reveal that citrate coated nanoparticles have a smaller magnetic diameter than the oleic acid coated ones. This is confirmed by the values obtained from magnetogranulometry in Table 4, which shows the results of the fitting. The magnetic volume fraction Φ_m (see eqn (12) below), mean magnetic diameter $\langle D_m \rangle = D_0 e^{\sigma^2/2}$ and magnetic diameter standard deviation

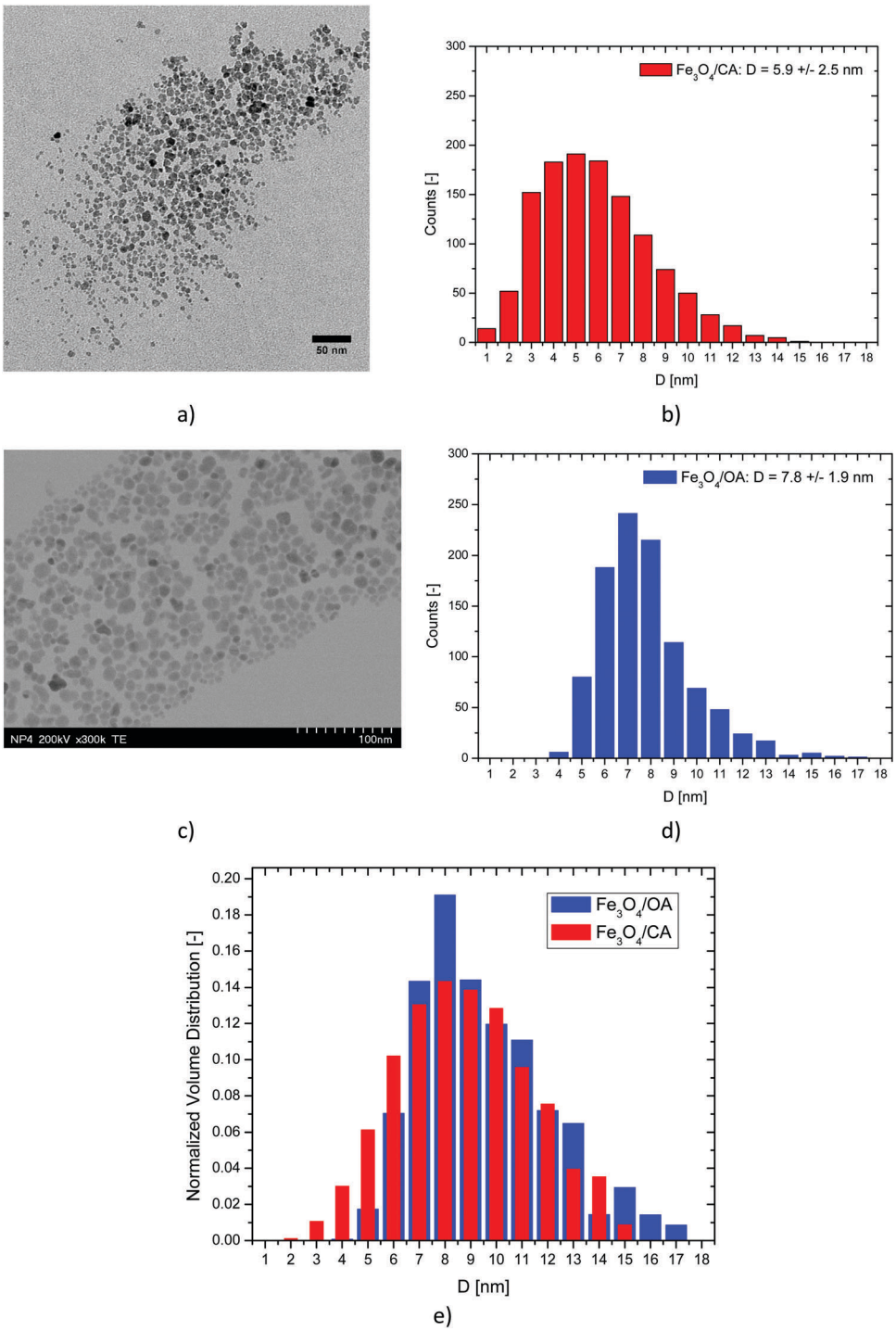

Fig. 2 TEM images and nanoparticle diameter histograms for: (a and b) Fe_3O_4/CA and (c and d) Fe_3O_4/OA samples; and (e) normalized volume distributions.

Table 3 Nanoparticle diameter (physical size) statistics calculated from TEM images for MF/CA and MF/OA stabilized ferrofluid samples

Sample	Number of particles	Mean [nm]	St. dev. [nm]	Skewness [–]
Fe_3O_4/CA	1215	5.9	2.5	0.6
Fe_3O_4/OA	1014	7.8	1.9	1.0

$\delta_m = D_0 e^{\sigma^2/2}\sqrt{e^{\sigma^2}-1}$ were calculated. The magnetic diameter of the nanoparticles is found to be 5.8 ± 2.3 nm for the Fe_3O_4/CA sample and 6.7 ± 2.7 nm for the Fe_3O_4/OA sample. The magnetic diameter is slightly smaller than the physical diameter, 5.9 ± 2.5 nm and 7.8 ± 1.9 nm, respectively, due to the nonmagnetic layer at the surface of the nanoparticles.[78]

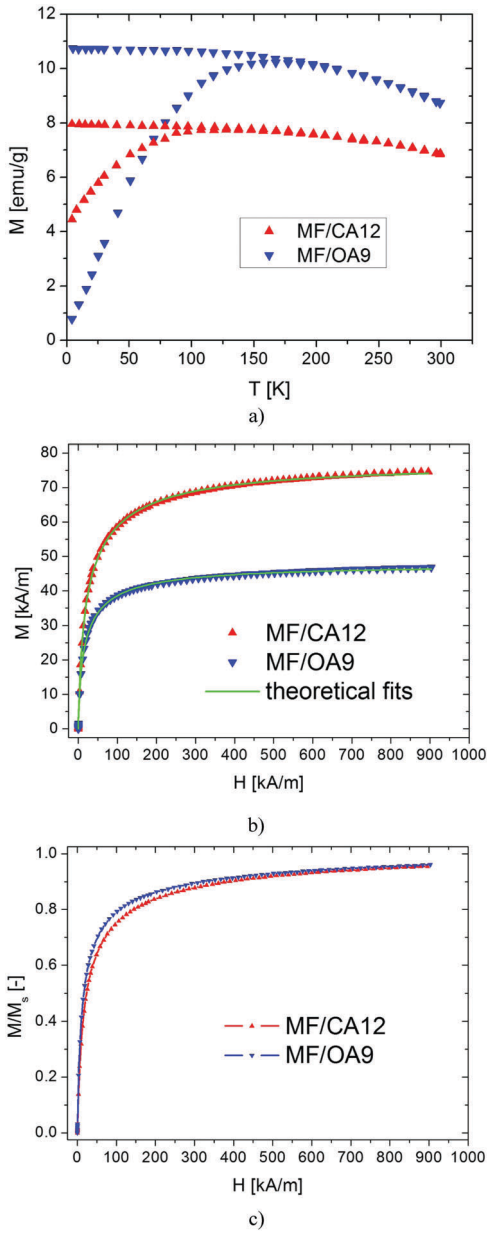

Fig. 3 Magnetic behaviour of the non-diluted MF/CA and MF/OA ferrofluids: (a) ZFC/FC; (b) comparative experimental and fitted room temperature magnetization curves, and (c) non-dimensional magnetization curves (corrected taking into account the demagnetizing field). The labels MF/CA12 and MF/OA9 correspond to the codes given in Tables 1 and 2.

Thus, TEM, magnetogranulometry and ZFC/FC magnetization curves all show that the citrate stabilized nanoparticles have smaller sizes/volumes than the OA stabilized ones.

The magnetic interactions in MF/CA12 and MF/OA9 samples can be compared using the ratio γ of the magnetic dipole–dipole energy over kT:[12]

$$\gamma = \frac{\mu_0 m^2}{\bar{r}^3 kT} = \frac{\mu_0 m_s^2 v}{kT}\Phi \quad (9)$$

where $\bar{r}$ is the average distance between nanoparticles' centers, $m = m_s^* v$ is the magnetic moment, $v = \pi d^3/6$ is the volume and $\Phi = v/\bar{r}^3$ is the solid volume fraction in the cubic lattice approximation. Eqn (9), rigorously valid for monodisperse magnetic nanoparticles, formally shows that $\gamma^* = \gamma/\Phi$ is independent of the sample volume fraction and depends only on the nanoparticle diameter. On the other hand, γ can be directly computed from the measured initial magnetic susceptibility χ_0 of the ferrofluid,[12] using an appropriate theoretical model for magnetization. The comparison of γ^* values gives an indication of the susceptibility for magnetically driven structuring in different ferrofluid samples.

For the purpose of our investigation, because the magnetization model in eqn (1) is expressed in terms of the nanoparticle magnetic diameter, γ will be expressed as a function of the magnetic volume fraction. Given the nanoparticle size polydispersity in MF/CA and MF/OA ferrofluids, $d\gamma$ and $d\Phi_m$ need to be defined for particles with diameters in the range (D_m, $D_m + dD_m$):

$$d\gamma = \frac{\mu_0 m_s^2 v_m}{kT}\cdot d\Phi_m; \quad d\Phi_m = v\cdot dn; \quad dn = n\cdot f(D_m)\cdot dD_m, \quad (10)$$

where n is the nanoparticle concentration and $f(D_m)$ is the magnetic diameter probability distribution function (see eqn (1)). Thus, γ can be expressed as an average over the diameter probability distribution function:

$$\gamma = \frac{\pi^2 \mu_0 m_s^2}{36kT} n \int D_m^6 f(D_m)\cdot dD_m \quad (11)$$

γ is proportional to the 6-th moment of the magnetic diameter distribution. Using the general formula of the log-normal distribution moments $\langle D_m^k\rangle = D_0^k \cdot \exp(k^2\sigma^2/2)$ and the expression of the volume fraction:

$$\Phi_m = \int d\Phi_m = n\frac{\pi}{6}\int D_m^3 f(D_m)\cdot dD_m = n\frac{\pi}{6}\langle D_m^3\rangle, \quad (12)$$

one gets:

$$\gamma = \frac{\pi\mu_0 m_s^2}{6kT}\langle D_m^3\rangle e^{9\sigma^2}\Phi_m. \quad (13)$$

Like in the monodisperse case, $\gamma^* = \gamma/\Phi_m$ is independent of the sample volume fraction and depends only on nanoparticle diameter statistics, here assumed to be log-normal. In the

Table 4 Saturation magnetization and nanoparticle diameter (magnetic size) statistics calculated from magnetization curves for CA and OA stabilized ferrofluid samples

Sample	χ_0 [−]	M_S [kA m^{-1}]	$M(1/H)$ lin. fit R^2	n [$\times 10^{22}$ part per m^3]	D_0 [nm]	σ [−]	Fit R^2	Φ_m [−]	$\langle D_m\rangle$ [nm]	δ_m [nm]
MF/CA12	3.07	78.20	0.996	86.72	5.35	0.39	0.9999	0.14	5.8	2.3
MF/OA9	3.68	48.73	0.991	39.91	6.23	0.39	0.9997	0.10	6.7	2.7

polydisperse case however, besides the average volume, γ^* also depends on the standard deviation σ. Because the log-normal skewness $\left(\mathrm{skw} = \left(e^{\sigma^2} + 2\right)\sqrt{e^{\sigma^2} - 1}\right)$ is a monotonically increasing function of σ and vice versa, γ^* accounts for the higher influence of large particles on the magnetic interactions taking place in the structure of ferrofluids.

By inserting eqn (13) in the low field approximation of eqn (1) (which is readily obtained using the Langevin function approximation $L(x) \cong x/3$ for small x) one obtains the following equation relating γ to the initial susceptibility of the ferrofluid:

$$\chi_0 = \frac{\gamma}{3} + \frac{\gamma^2}{27} + \frac{\gamma^3}{3888}. \quad (14)$$

Using the samples' initial susceptibilities (Table 4) and magnetic volume fractions determined with eqn (12) (Table 4), γ^* was calculated to be 40.6 for MF/CA12 and 63.4 for MF/OA9. One can notice that γ^* is much larger for MF/OA9, which shows higher susceptibility for magnetically driven structuring in MF/OA9 than in MF/CA12.

Using eqn (12) for the magnetic volume fraction, the thickness r_{nm} of the nonmagnetic layer can be calculated from the physical Φ and magnetic Φ_m volume fractions. If one assumes that the physical and magnetic diameter log-normal distributions have the same σ, but the mode D_{0p} of the physical diameter is $2*r_{nm}$ larger than the mode D_{0m} of the magnetic diameter ($D_{0p} = D_{0m} + 2*r_{nm}$), the thickness of the nonmagnetic layer is 0.35 nm for MF/CA12 and 0.37 nm for MF/OA9. This result, bearing in mind that the nanoparticles in both ferrofluids were synthesized by means of co-precipitation, shows that the thickness of the nonmagnetic layer is not influenced by the nature of the adsorbed molecules at the surface of the nanoparticles, *i.e.* citric acid and oleic acid, respectively. Moreover, taking into consideration the dependence on the thickness of the surfactant layer r_s of the maximum magnetic dipole–dipole interaction parameter per particle:

$$\lambda = \frac{\pi\mu_0 m_s^2}{144kT} \cdot \frac{D_m^6}{(D_m + 2r_{nm} + 2r_s)^3} \quad (15)$$

it follows that the magnetic interparticle correlations increase with decreasing surfactant layer thickness.

3.3. Particle surface properties: XPS and ATR-FTIR analyses

Fig. 4 and 5 show high resolution XPS spectra of Fe2p, C1s and O1s for dried samples of the magnetic nanofluids Fe_3O_4/CA and Fe_3O_4/OA, respectively. Applying a similar analysis as in ref. 79, the deconvolution of these spectra shows the contributions from the peaks assigned to specific groups of the surfactants oleic acid or citric acid, and from magnetite.

The Fe2p spectrum contains the doublet Fe2p3/2 and Fe2p1/2. The best fit for the Fe2p spectrum was obtained with the components corresponding to Fe^{2+} octahedral, Fe^{3+} octahedral, and Fe^{3+} tetrahedral, respectively, and the satellites, in agreement with the reported data.[80,81]

For the Fe^{3+}/Fe^{2+} atomic concentration ratio calculated from the Fe^{3+} and Fe^{2+} peak areas we obtained values which are close to that expected for magnetite: $Fe^{3+}/Fe^{2+} = 2.2$ for Fe_3O_4/OA and $Fe^{3+}/Fe^{2+} = 2.08$ for Fe_3O_4/CA. For each sample the fitting parameters including the peaks positions, FWHM, and calculated atomic concentrations for the Fe2p components are given in Table 5. The best fit of C1s spectra for the nanofluid samples was obtained with 3 components (Fig. 4 and 5): the most intense component located at the binding energy 284.7 eV corresponds to C–C, and C–H groups; the component located around 286 eV corresponds to C–O attributed to the monodentate bond of carboxylate from oleic acid (OA) or citric acid (CA), respectively; and the higher binding energy component located at 288.4 eV corresponds to the bidentate bond of carboxylate from the surfactant[80] and to the carboxylate from the free surfactant molecules in the nanofluid samples. The intensity of the band located at 288.4 eV is higher for the Fe_3O_4/CA sample in comparison with Fe_3O_4/OA due to the higher concentration of carboxyl groups.

For both nanofluid samples the oxygen spectra exhibit 3 components (Fig. 4 and 5) assigned to Fe–O from magnetite (530 eV), C–O/C=O (531.7 eV for Fe_3O_4/OA and 531.1 eV for Fe_3O_4/CA) which corresponds to monodentate carboxylate oxygen atoms, and O–C=O (533 eV) corresponding to oxygen atoms in the bidentate bond at the magnetite surface and to the carboxylate from the free surfactant molecules in the nanofluid samples.

The XPS analysis confirms that the facile coprecipitation process under atmospheric conditions applied in this work provides preponderantly magnetite nanoparticles, *i.e.* without

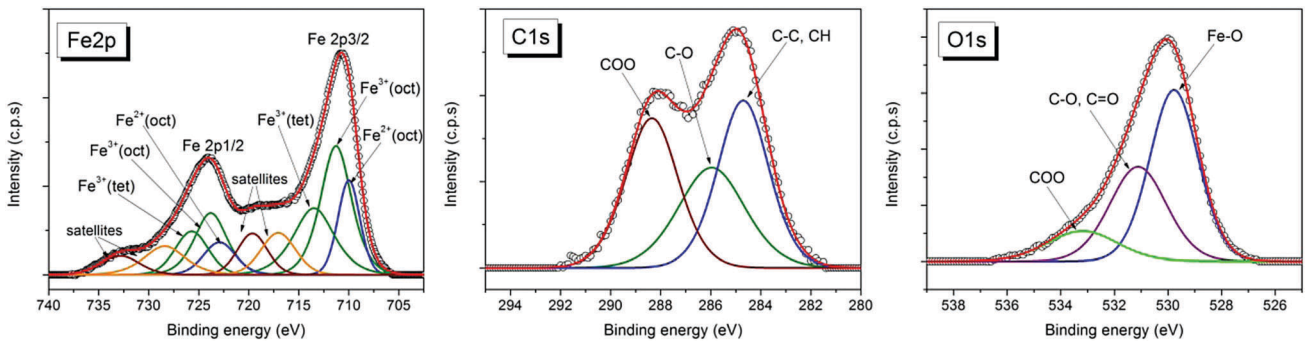

Fig. 4 Fe2p, C1s and O1s XPS spectra for Fe_3O_4/CA.

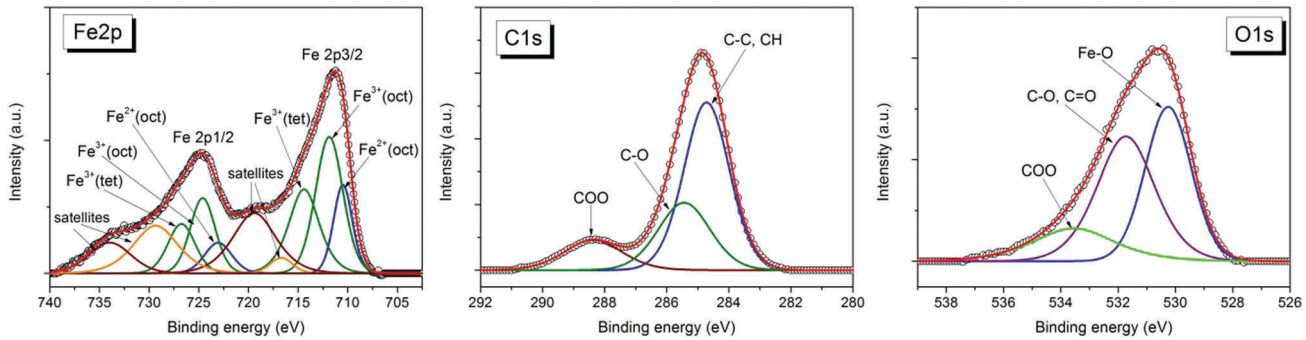

Fig. 5 Fe2p, C1s and O1s XPS spectra for Fe_3O_4/OA.

Table 5 Fitting parameters, including peaks positions, FWHM and calculated atomic concentrations from peak areas of Fe2p XPS spectra for the dried samples Fe_3O_4/OA and Fe_3O_4/CA

	Position (eV)	FWHM (eV)	Atomic conc. (%)	Position (eV)	FWHM (eV)	Atomic conc. (%)
Peak name	Fe_3O_4/OA			Fe_3O_4/CA		
Fe^{2+} 2p3/2 (octahedral)	710.5	2.2	6.44	710	2.5	8.499
Fe^{3+} 2p3/2 (octahedral)	711.8	3.2	14.535	711.2	3.6	17.122
Fe^{3+} 2p3/2 (tetrahedral)	714	3.6	10.343	713.5	4.7	11.717
Fe^{2+} 2p1/2 (octahedral)	723	3.2	6.234	723	3.7	8.228
Fe^{3+} 2p1/2 (octahedral)	724.6	2.9	14.072	724	3.8	16.575
Fe^{3+} 2p1/2 (tetrahedral)	726.7	3.2	10.012	725.7	3.8	11.341
Fe^{2+} 2p3/2 satellite	716.6	2.6	1.344	717	4	5.913
Fe^{3+} 2p3/2 satellite	719.4	5.1	10.527	719.6	3.5	5.083
Fe^{2+} 2p1/2 satellite	729.3	5.3	16.736	728.4	4.8	9.725
Fe^{3+} 2p1/2 satellite	733.9	5	9.756	732.8	4.5	5.798

the oxygen-free reaction medium frequently considered during synthesis, such as Ar[24] or N_2,[82] to ensure formation of magnetite instead of other iron oxides.

FTIR spectra for the electrostatically stabilized magnetic fluid MF/CA (FTIR absorbances: 1583, 1390, and 530 cm^{-1}), uncoated iron oxide nanoparticles (FTIR absorbances: 3113, 3011, 2805, 1757, 1394, and 570 cm^{-1}) and citric acid (FTIR absorbances: 1566, and 1389 cm^{-1}) are presented in Fig. S1 (ESI†). The pHs of the uncoated NP and citric acid solutions were adjusted to ~7 (the pH of the MF/CA) with HCl and NaOH, respectively. The citric acid spectrum shows the asymmetric (1566 cm^{-1}) and the symmetric (1389 cm^{-1}) stretching bands of the carboxylate group. For MF/CA the asymmetric peak of adsorbed citric acid is moved to a higher wavenumber (1583 cm^{-1}) indicating the formation of direct metal-carboxylate complexes.[79]

Similar spectra for electro-sterically stabilized magnetic fluid MF/OA (FTIR absorbances: 2918, 2849, 1631, 1536, 1403, and 559 cm^{-1}), uncoated iron oxide nanoparticles (FTIR absorbances: 3113, 3002, 2802, 1754, 1390, and 552 cm^{-1}) and oleic acid (FTIR absorbances: 2922, 2851, and 1561 cm^{-1}) are presented in Fig. S2 (ESI). The pHs of the uncoated NP and oleic acid solutions were adjusted to ~9 (the pH of the MF/OA) with HCl and NaOH, respectively.

The Na-oleate spectrum shows the aliphatic R′–CH_2–R″ stretching bands at 2922 and 2851 cm^{-1}, which are also present in the MF/OA spectrum at the same positions. The carboxylate R–COO^- stretching of oleic acid (1561 cm^{-1}) moved to a lower wavenumber (1536 cm^{-1}) in MF/OA, while the symmetric one remains almost unchanged (1403 cm^{-1}). In the MF/OA spectrum, the difference between the asymmetric and symmetric COO– peaks is 133 cm^{-1}, which reveals bidentate type coordination of R–COO^- on the iron oxide surface.[83,84] The 1631 cm^{-1} peak in the MF/OA spectrum is assumed to come from a small amount of residual water in the dried sample.

Both types of magnetic fluids and uncoated NPs show a single peak at 530–570 cm^{-1}, which is consistent with Fe_3O_4 (a peak near 570 cm^{-1}). Furthermore, the spectra are missing peaks at 470 cm^{-1}, which suggests that the iron oxide in the samples is not α-Fe_2O_3. Similarly, the absence of additional peaks between wavenumbers 600 and 700 cm^{-1} suggests that the crystal form is not γ-Fe_2O_3.[85]

3.4. Colloidal stability: dynamic light scattering

The hydrodynamic diameter (*Z*-average) and the zeta potential for diluted samples of both types were measured as a function of pH in the range 3 to 11. The oleate and citrate stabilized magnetic fluid samples were stable almost over the whole pH range studied here except the most acidic pHs below 5 and 6, respectively.

Over the stable pH range, we obtained hydrodynamic diameters between 52 and 110 nm for the citric acid covered particles with a PDI of 0.26–0.46, and between 98 and 147 nm for the oleic acid covered particles with a PDI of 0.12–0.23. The citrate covered particles thus have smaller *Z*-average particle sizes than the oleic acid covered nanoparticles. The most acidic

samples were unstable and started to coagulate right after sonication. The corresponding sizes, ~1000 nm and ~1400 nm, measured for oleate and citrate stabilized samples (Fig. 6 and 7), respectively, are thus only characteristic of the given kinetic stage. These samples settle down over a time of a few hours. It should be noted that the diameters calculated from DLS include the effect of a hydration layer around the particles. The thickness of this layer can be relatively large, with the result that the DLS sizes will generally be higher than those obtained from the SAXS and SANS analysis (presented later).

Zeta potentials measured for the citrate and oleate stabilized samples show the characteristic pH-dependence due to the different dissociation behaviors of the acidic groups on the coating molecules.

Both samples are seen to be stable over a wide pH range; however, the MF/CA sample loses colloidal stability below pH 6, while the MF/OA sample below pH 5, because of the difference in the charge state of these coated nanoparticles due to different dissociability (the citric acid has: pK_{a1} = 3.13, pK_{a2} = 4.76, and pK_{a3} = 6.40, while the oleic acid has pK_a = 5.02). The charging behaviour of OA double layer stabilized MNPs can be understood considering its pK_a value. At pH ~ 5, the zeta potential is still high (−50 mV) for the oleic acid sample, and the particles are charged, since about the half of oleic acid molecules in the 2nd layer are dissociated. However, the potential is significantly decreased below this limit. The system then loses its stability, the particles start to aggregate, and the average particle size increases abruptly. The citric acid is bound to the MNP *via* one of its –COOH groups that connects to ≡Fe–OH sites on the surface.[61] Dissociation of surface complexed citric acid differs from that of molecules dissolved in water (see pK_a values above), so charging of citrated MNPs is supressed below pH ~ 6, where the absolute value of the zeta potential drops just below 25 mV. We measured positive values of the zeta potential (5–15 mV) at and below pH 4 for the MF/CA samples (~5–10 mV in Fig. 6) and below pH 3.5 for the MF/OA sample (~15 mV in Fig. 7). These were not high, but systematic and above the reproducibility level (±5 mV) of this method. Under acidic conditions, positive zeta potential values are characterisitic of naked MNPs.[34] The results here thus indicate incomplete coverage of MNPs, as has been shown for citrated

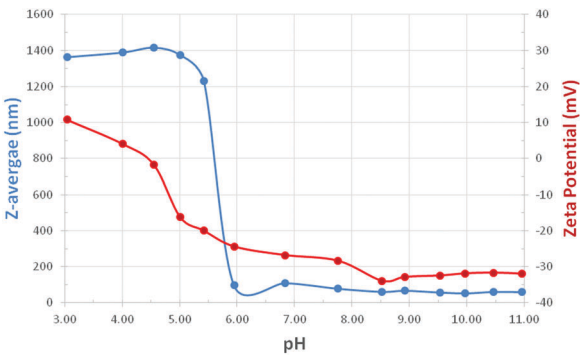

Fig. 6 pH dependence of the *Z*-average particle diameter (blue) and the zeta potential (red) for the citrated (MF/CA) sample.

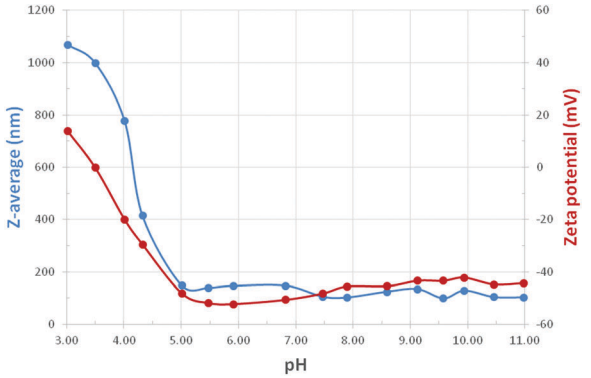

Fig. 7 pH dependence of the *Z*-average particle diameter (blue) and the zeta potential (red) for the oleic acid double layer stabilized (MF/OA) sample.

MNPs containing less than ~1 mmol COOH/g magnetite (*i.e.*, ~0.33 mmol CA was added to 1 g MNP)[61] and for oleate coated MNPs with an added OA amount lower than 1.5 mmol g^{-1}.[29] On the other hand, incomplete coverage of the present citrated sample is not very likely, since CA was added in high excess to the magnetite during synthesis as explained in point 2.2. For the MF/OA sample, the existing free surfactant in solution is conditioning the formation of a physisorbed secondary OA layer which gives the hydrophilic character of dispersed magnetite NPs. The resulting degree of coverage is dependent on the added amount of OA during synthesis (given in point 2.3).

3.5. Structure

3.5.1. Electrostatically stabilized magnetic fluids analyzed by SAXS and SANS. SAXS and SANS data obtained for citric stabilized magnetic nanoparticles with the volume concentration of MFs varying from 0.5 to 20% are shown in Fig. 8. The scattering intensities have been normalized to the concentration of MNPs, which gives the possibility for direct comparison of size and interaction among MNPs (or their aggregates), depending on the concentration.

The SAXS and SANS data both show a continuous decrease of the normalized scattering intensity in the low-*q* region with increasing MNP concentration, suggesting that the MNPs show dominating repulsive interaction and do not aggregate into larger complexes. This concentration dependence is thus an indication that the magnetic fluids are stable in the studied concentration range. The shape of curves for SAXS and SANS is quite similar, indicating only minor differences in the X-ray and neutron scattering length density profiles for these particles in H_2O. This is corroborated by the calculated scattering length densities (Table 6), and that there is only a very small contribution of magnetic scattering for SANS in these conditions. The log–log slope at high *q*-values is found to be close to −4, showing that the particle surface is smooth at short length scales for all concentrations studied.

Based on this initial inspection of the scattering data, one can proceed with model fitting. We first tried to describe the scattering curves using a model with individual polydisperse particles (log-normal distribution) as had been observed by

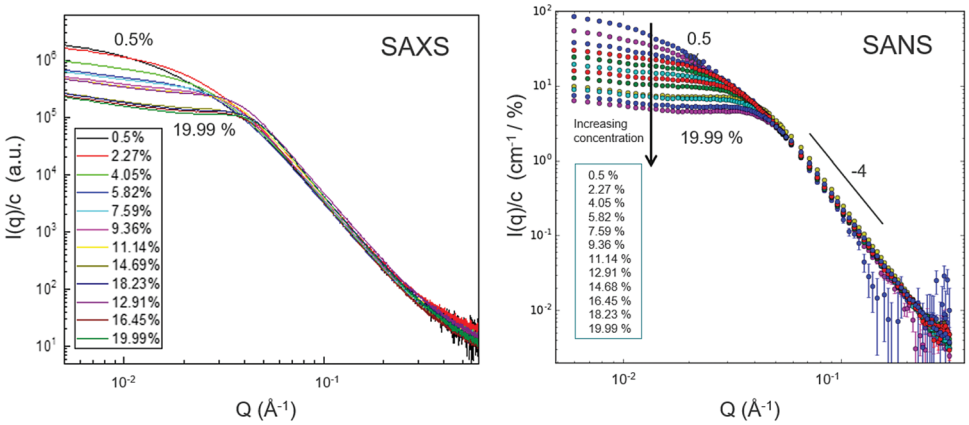

Fig. 8 SAXS and SANS intensities normalized to the concentration of MNPs (Fe_3O_4/CA) with varying concentration. The SANS data have been background-subtracted for the H_2O contribution.

Table 6 Scattering length densities (SLD) for the different components calculated using the SLD calculator in the SasView program[86]

	Fe_3O_4	H_2O	Citrate	Oleic acid
SAXS [Å^{-2}] × 10^{-6}	40.3	9.42	14.7	8.5
SANS [Å^{-2}] × 10^{-6}	6.93	−0.56	3.3	0.078

TEM (Fig. 2). However, it was not possible to obtain reasonable fits in this way, even when including an interaction potential. On the other hand, a model of prolate ellipsoids of rotation with polydispersity in the small axis, including screened Coulomb interaction did produce satisfactory fits, see Fig. 9.

In the modelling we minimized the number of free fitting parameters, fixing values that are known from other methods or calculations (*cf.* SLD-values in Table 6). The shape (log-normal) and width of the distribution of the small axis were fixed to the values obtained for the MNPs from TEM. The thickness of the citric acid layer was fixed to 4 Å, which was the converging value obtained from the fit of SANS data at the lowest concentration (0.5%) where the particle interactions can be neglected. The parameters resulting from the fitting are thus the small axis, the axial ratio, and the magnitude of the surface electrical charge; see fitted values for selected concentrations in Table 7. One should note that since the SANS data are normalized to an absolute scale (cm^{-1}), it is possible to verify if the total scattered intensity corresponds to what is expected from a given volume fraction of the magnetic particles. For all concentrations measured, the data fitted well to a model with a volume fraction fixed to the nominal value known from the preparation protocol, demonstrating that if any large agglomerates (outside the accessible range for SANS) exist in the sample, the amount of these must be very small.

The results from SAXS and SANS thus point towards the presence of short MNP aggregates in the form of ellipsoids of revolution, consisting of a moderate number (3–6) of MNPs and carrying a relatively low electrical charge. The aggregates become shorter with increasing concentration, and at the same time the interaction between aggregates becomes stronger. A plot of the particle axial ratio as well as the charge based on the SAXS data is shown in Fig. 10.

We can also get information about the interactions in the system, *i.e.* the structure factor, by dividing all higher concentration data with one of the lowest concentrations where the

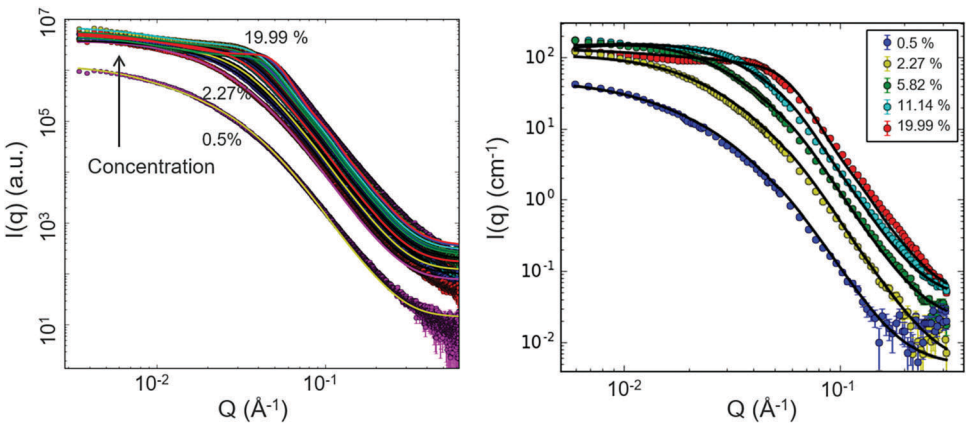

Fig. 9 SAXS (left) and SANS data (right) of Fe_3O_4/CA magnetic fluids with fits (continuous lines) using a core–shell ellipsoidal model and a screened Coulomb interaction potential. Only selected concentrations are shown for the SANS data in order to better appreciate the difference between the curves with increasing concentration.

Table 7 Values for the core radius (equatorial) and the axial ratio for the model particle (ellipsoidal core–shell) as well as the effective charge in the Hayter-Penfold structure factor for the Fe_3O_4-citrate system at selected concentrations. The st. dev. in *R* core is ±0.5 Å, in the axial ratio ±0.2, and in the effective charge ±0.2. The inset is a simple sketch of an arrangement of particles that could give a resulting scattering pattern consistent with the model

Conc. [%]	*R*_core [Å]	Axial ratio	Eff. charge [e^-]
0.5, SANS	21.8	3.8	0
SAXS	22.3	6.1	0.1
2.27, SANS	21.8	2.3	0.2
SAXS	22.3	7.9	1.8
5.82, SANS	22.2	2.6	2.3
SAXS	22.3	6.1	2.2
11.14, SANS	22.3	3.4	5.1
SAXS	22.3	5.3	3.3
19.99, SANS	22.1	3.3	8.9
SAXS	22.3	4.6	4.1

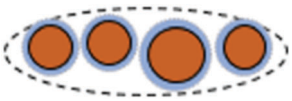

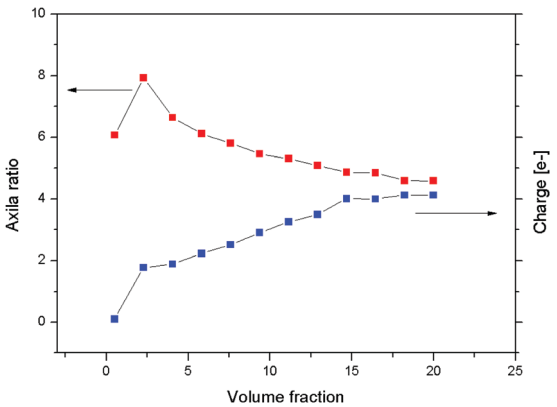

Fig. 10 Axial ratios and effective particle charge of Fe_3O_4/CA particles as extracted from the modelling (SAXS data).

interactions are negligible (the latter representing the form factor). In Fig. 11 is shown a plot of this "apparent" structure factor (based on the SANS data), where all data have been divided by the data for the sample with a concentration of 2.27%, since at that concentration the interactions were found to be very small. The particle interactions give rise to a correlation peak in the SANS data (that was seen best for the very highest concentration) which can now also be identified as the position where the relative intensity changes from a sharply rising curve to a plateau-behavior. With this plot, it is quite easy to see how this deflection point moves continuously to higher *q*-values, *i.e.* smaller distances, as the concentration is increased. This is an additional sign that as the concentration is increased, aggregation of our primary entities (*cf.* sketch in Table 7) is not taking place, but instead there are continuously more particles present per volume unit.

3.5.2. Electro-sterically stabilized magnetic fluids (Fe_3O_4/OA) analyzed by SAXS and SANS

SAXS. SAXS data obtained for oleic acid stabilized MNPs with volume concentration varying from 0.5 to 9.5% are shown

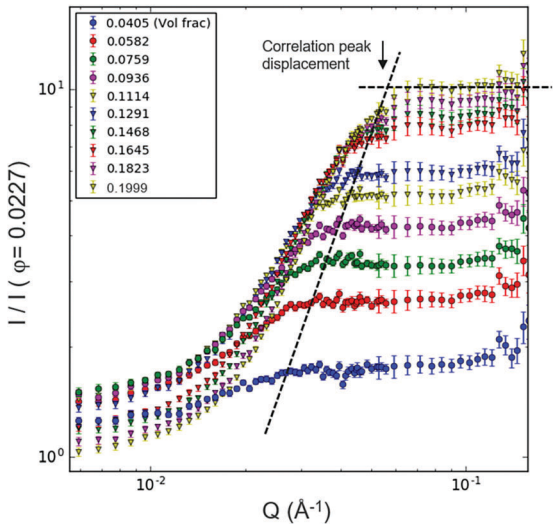

Fig. 11 Plot of the "apparent" structure factor for magnetic fluids with Fe_3O_4/CA particles. The SANS data have been divided by the data for a low-concentration MF/CA sample (a concentration of 2.27%, volume fraction φ = 0.0227), without any further scaling.

in Fig. 12. SANS data were also collected for this system after the SAXS measurements. However, for these samples there were signs of aggregation having taken place in-between the SAXS and SANS measurements (in contrast to the citric acid stabilized MNPs), resulting in an increase in the intensity at low *q*-values. The SANS data will thus be treated separately and commented on later.

It is reasonable to start the modeling of the SAXS data with the low-concentration sample (0.5%), where interactions between the different model particles are not important. As can be seen clearly in Fig. 12 (right), the 0.5% system does not show a low-*q* plateau, but instead a slope of *ca.* −1.0 (log–log) in this *q*-range. This indicates elongated structures, with a large axial ratio, *i.e.* cylinder-like. A core–shell cylinder model gave a good fit to the data, as shown in Fig. 12, right panel. The length was fitted to 197 nm, and the core radius to 2.8 nm, *i.e.* slightly smaller than the mean particle radius found from TEM. With a shell thickness (OA coating) of approx. 3 nm, this is equivalent to an axial ratio of *ca.* 16.9, or about 16 particles (on average) "linked" together at this low concentration.

At concentrations above 2%, we found that the cylinder model produced shorter axial ratios and did not give very good fits to the data. With shorter axial ratios, it may in fact be more reasonable to employ an ellipsoidal model instead of a cylinder, similarly to what was found for the citric acid (CA) stabilized system. With this model, we could obtain quite good fits, see in Fig. 13 for some selected data. However, some variation in the fitted core radius was found between the different concentrations. The axial ratio was found to be *ca.* 7 : 1 at 2%, decreasing to 4 : 1 for the highest concentration. One should note that for the oleic acid stabilized MNPs, the volume fraction ends up at a value considerably higher than the nominal value. Since the latter is given based on the non-coated material, this observation is as expected. For the 9.5% concentration (nominal value), the effective volume fraction was fitted to 21%, thus an increase

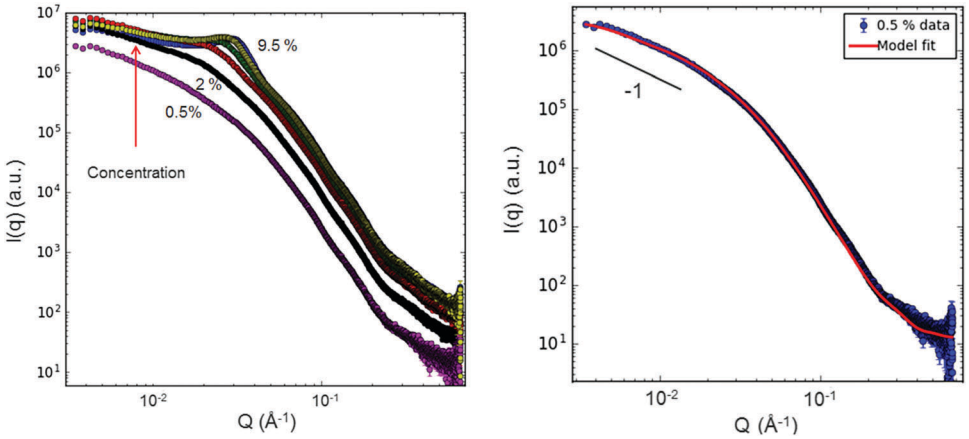

Fig. 12 SAXS data (left) for oleic acid stabilized magnetic fluids with concentrations from 0.5 to 9.5%. The fit to the low concentration sample (0.5%) using a cylinder model is shown to the right.

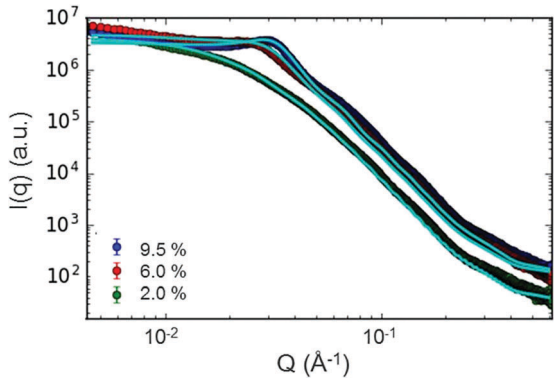

Fig. 13 Fits to SAXS data for oleic acid stabilized magnetic fluids with volume concentrations of 2, 6 and 9.5% using an ellipsoidal core–shell model.

Table 8 Values for the core radius (equatorial) and the axial ratio for the model particle (cylinder core–shell at 0.5% and ellipsoidal core–shell at higher concentrations) as well as the effective volume fraction using a hard-sphere structure factor for the Fe_3O_4/OA system at selected concentrations. The st. dev. in *R* core is ±0.5 Å, in the axial ratio ±0.2, and in the effective charge ±0.2

Conc. [%]	*R*-core [Å]	Axial ratio	Eff. vol. fraction [%]
0.5, SAXS	28.4	16.9	0.5
2.0, SAXS	24.5	7.8	4.1
4.0, SAXS	33.1	7.6	7.8
6.0, SAXS	25.1	6.9	17.2
8.0, SAXS	33.6	4.7	17.8
9.5, SAXS	34.3	3.9	21.4

with a factor of about 2.2 due to the hydration and steric effects of the oleic acid double layer coating (Table 8).

We are thus able to fit the SAXS data quite well for all concentrations with an ellipsoidal model (cylinder for the lowest concentrations) and using a simple hard-sphere potential. This is probably due to that fact that the steric repulsion from the OA–OA layer dominates strongly over any charge effects. It is worth to emphasize that by applying the factor of 2.2 mentioned above for the most concentrated MF/OA9 sample, the effective (hydrodynamic) volume fraction of OA coated magnetite NPs attains 30%, which is practically the same as for the highest concentration of the CA stabilized sample considering a 0.4 nm thickness of the CA coating.

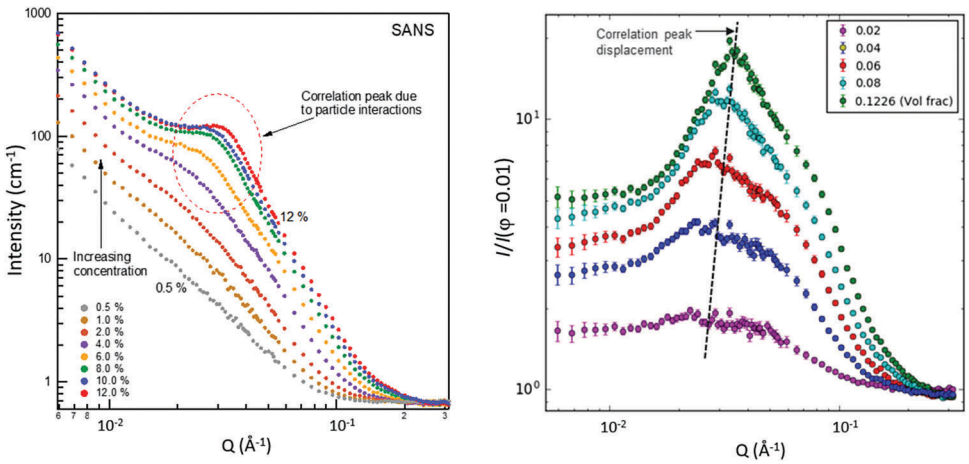

Fig. 14 SANS data for the Fe_3O_4/OA aqueous MF at different concentrations (left). Plot of the "apparent" structure factor (right). The SANS data have been divided by the data for a low-concentration sample (1%), without any further scaling.

Time-dependent effects – SANS. As mentioned earlier, the SANS data for this system showed excess scattering at low q-values, with a steep slope indicating the presence of aggregated structures (see Fig. 14 left). Thus, an aggregation process seems to have taken place in the period between the SAXS and SANS data collection (*ca.* 6 months). These data were therefore not modelled in the same way as the SAXS data. However, a plot of the apparent structure factor is shown in Fig. 14 (right), where the SANS data have been divided by the data at low-concentration. This plot shows the appearance and systematic strengthening of the correlation peak with increasing concentration, and also how this peak is displaced systematically to higher q-values with increasing concentration. The latter is as expected since it shows the continuously reduced interaction distance between entities.

3.6. Magnetorheology

Magnetorheology clearly differentiates between the two types of magnetic fluids, with electrostatic (MF/CA) and electro-steric (MF/OA) stabilization.

For the most concentrated oleic acid stabilized magnetic fluid sample (MF/OA9), shear-thinning (pseudoplastic) behavior both in zero and non-zero magnetic fields is observed (Fig. 15). This indicates that the sample contains agglomerates which are progressively destroyed at increasing shear rate values. The sample manifests a magnetoviscous (MV) effect, *i.e.* the applied field induces the formation of new agglomerates, besides those already existing in zero field. After demagnetization the viscosity values remain slightly increased with respect to the initial values. This shows that the agglomerates formed in the applied field do not fall apart when the field is switched off (are irreversible at the characteristic timescale of measurements).

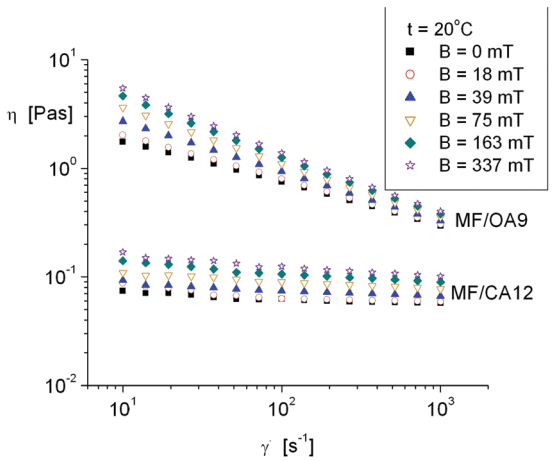

Fig. 15 Viscosity curves for the highest concentration MF/CA (physical vol fraction 20%) and MF/OA (physical vol fraction 14%) samples at different magnetic field strengths.

For the citric acid stabilized highest concentration magnetic fluid sample (MF/CA12), we observe approximately Newtonian behavior in zero and non-zero magnetic field (Fig. 15). The magnetoviscous effect is reduced and practically independent of the shear rate. Furthermore, the magnetic field induced agglomeration of particles is partly irreversible; after demagnetization the viscosities are somewhat higher than the initial values. Moreover, at B = 337 mT the sample becomes slightly pseudoplastic.

The magnetoviscous effect $\frac{\Delta\eta}{\eta(0)} = \frac{\eta(B) - \eta(0)}{\eta(0)}$ for all values of the shear rate investigated is represented in Fig. 16a and b which are analyzed below.

For the oleic acid stabilized MF sample (MF/OA9) the MV effect is reduced for increasing shear rate values; *i.e.* continuously more agglomerates are destroyed. For the citric acid sample (MF/CA12) the MV effect is found to be small and practically independent of the shear rate. Here the field induced agglomerates remain also at high shear rate values.

For the magnetic field dependence of the MV effect illustrated in Fig. 16b, the experimental values are correlated with a power-law dependence:

$$\frac{\Delta\eta}{\eta(0)} = aB^n \qquad (16)$$

For small shear rates the magnetoviscous effect is considerably higher for the MF/OA9 sample. By increasing the shear rate to above 10^2 s^{-1} the situation changes and the MV effect is somewhat greater for the MF/CA12 sample. This indicates the

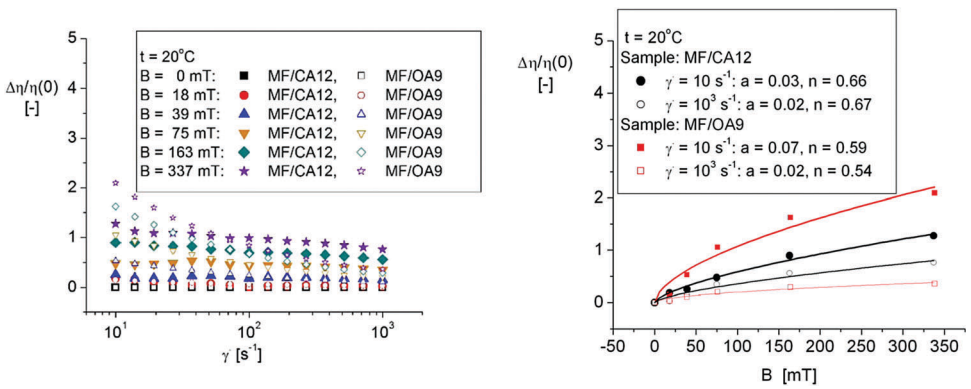

Fig. 16 (a) Magnetoviscous (MV) effect: dependence on the shear rate. (b) Magnetoviscous effect: dependence on the magnetic induction at $\dot{\gamma}$ = 10 s^{-1} and at $\dot{\gamma}$ = 10^3 s^{-1}.

existence of loosely bound agglomerates in the OA stabilized sample, which are disrupted by increasing the shear rate. There is no evidence of magnetic field induced phase separation that would give rise to abrupt and irreversible variation of the effective viscosity. The magnetoviscous behavior of the citric acid stabilized magnetic fluid sample is determined mainly by the physical particle volume fraction, which is significantly (approx. two times) higher than the oleic acid stabilized sample. The magnetoviscous effect, which was found to be more pronounced for the MF/OA9 sample at low shear rate than for the MF/CA12 sample, denotes the presence of agglomerates (the existence of correlations) already at small volume fraction values in the case of MF/OA magnetic fluids, as was evidenced by small-angle scattering. Nevertheless, the effective viscosity increase is moderate compared to the more than an order of magnitude increase observed in the case of bio-ferrofluids.[43]

4. Summary and conclusions

In this work we have employed a large range of techniques to characterize the two different magnetic fluids synthesized. These are water based high-concentration magnetic fluids with either electrostatic or electro-steric stabilization. In order to put the different methods and characteristics into an overall context, the following scheme (Fig. 17) gives a concise representation of the main properties of each type of particle/fluid (including the synthesis route), the kind of information extracted, and the corresponding experimental technique employed. Some potential applications for each magnetic fluid are also given.

As described in the main text, both types of samples, MF/CA with electrostatic and MF/OA with electro-steric stabilization, were obtained by applying a coprecipitation synthesis process under atmospheric conditions. For the Fe^{3+}/Fe^{2+} atomic concentration ratio, calculated from the Fe^{3+} and Fe^{2+} peak areas of XPS spectra, the obtained values are close to that expected for magnetite: $Fe^{3+}/Fe^{2+} = 2.2$ for the Fe_3O_4/OA sample and $Fe^{3+}/Fe^{2+} = 2.1$ for the Fe_3O_4/CA sample. Also, ATR-FTIR spectra for both types of magnetic fluids and uncoated NPs show a single peak at 530–570 cm^{-1}, which is consistent with Fe_3O_4 (a peak near 570 cm^{-1}). The facile synthesis procedure in the presence of oxygen applied in this work, giving about 50 grams of surface coated magnetite NPs/batch, proved to be highly efficient to produce water based ferrofluids. The saturation magnetization values 78.20 kA m^{-1} for electrostatically and 48.73 kA m^{-1} for electro-sterically stabilized aqueous ferrofluids, are among the highest values achieved up to now. While the saturation magnetization values are quite different, the hydrodynamic volume fraction of the most concentrated MF/CA and MF/OA samples is practically the same, approx. 30%, due to significantly different thicknesses of the particle surface coating layers. The non-dimensional magnetization curves reveal that nanoparticles in the MF/CA sample have smaller magnetic diameters than those dispersed in the OA stabilized MF sample. This is confirmed by the values of the magnetic size obtained from magnetogranulometry, 5.8 ± 2.3 nm for the MF/CA sample and 6.7 ± 2.7 nm for the MF/OA sample. The mean magnetic diameter is slightly smaller than the mean physical diameter as observed from TEM, 5.9 ± 2.5 nm and 7.8 ± 1.9 nm respectively, due to the nonmagnetic layer at the surface of the nanoparticles. Consequently, the non-dimensional magnetic interaction parameter, taking into account the average sizes, is well below 1 for both types of samples. However, the polydispersity evidenced by size distribution data (Tables 3 and 4) and also DLS sizing (PDI between 0.12 and 0.46 from cumulant analysis for diluted MFs in the colloidally stable pH region) show the existence of a fraction of relatively large (over 10 nm) particles whose magnetic interaction exceeds the thermal energy and favors chain formation. Indeed, the SAXS and SANS results point towards formation of short chains of

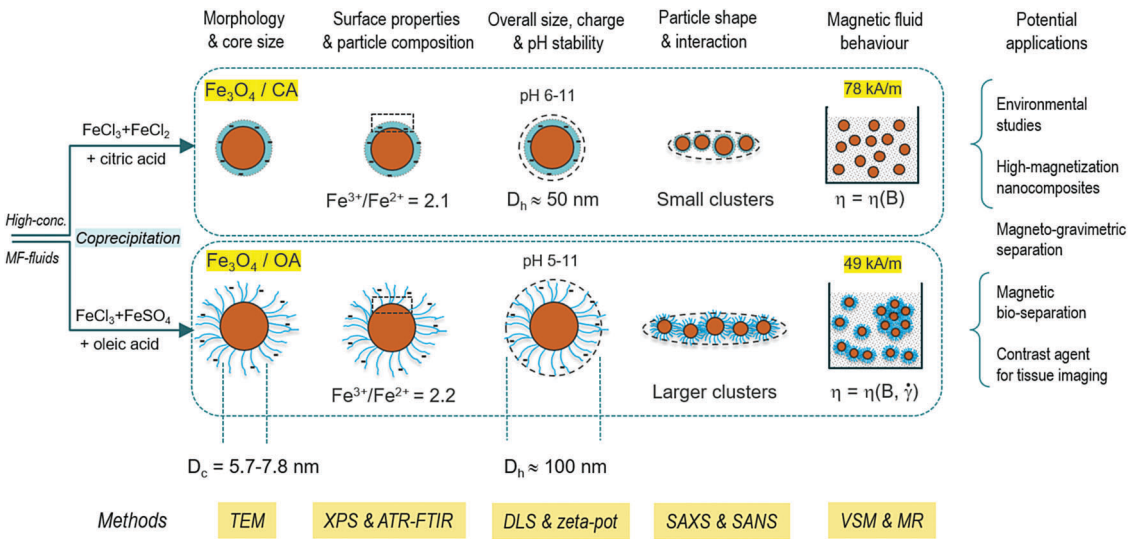

Fig. 17 Comparison of electrostatically and electro-sterically stabilized concentrated aqueous magnetic fluids.

magnetic nanoparticles (less than 10 primary particles) which are relative stable against coagulation with increasing concentration. Even some decrease of apparent chain length with concentration could be observed from the fitting parameters. Interaction among these chains is mostly due to excluded volume interaction for the OA stabilized system and electrostatic interaction in the case of CA stabilization. In the plot of the apparent structure factor, the correlation peak moves continuously to higher q-values with increasing particle concentration. It shows a plateau-behavior for MF/CA and a systematic strengthening of the correlation peak for MF/OA samples, which reflects particle aggregation in the case of the electrosteric stabilized MF/OA samples. The citrate covered particles have a smaller Z-average diameter than the oleic acid covered nanoparticles over a broad range of pH values, where both samples are stable. However, the citrated sample loses colloidal stability below pH 6, whereas the oleic acid double layer stabilized sample below pH 5, because of the difference in the charge state of organic acid coated MNPs.

The OA stabilized MF sample manifests shear-thinning (pseudoplastic) behavior both in zero and non-zero magnetic fields, while the MF/CA sample has approximately Newtonian behavior both in zero and non-zero magnetic fields. This is indicated in the illustration above, with the viscosity being labeled as without shear-rate dependence. Such a difference between the two fluids can certainly be important in terms of applications, especially where flow fields are encountered. Abrupt changes of the effective viscosity in magnetic fields, which would reflect magnetic field induced phase separation, were not observed. Magnetorheology, in good correlation with the results from small-angle scattering, clearly differentiates the two MF water samples concerning their structure and evidences field and shear rate dependent loosely bound structures in MF/OA, which was not the case for the MF/CA sample. As a consequence, for higher values of the shear rate the situation changes and the magnetoviscous effect is somewhat larger for the MF/CA sample. In the case of MF/OA samples the particle correlation effects and cluster formation evidenced by SAXS and SANS already at 1–2% physical volume concentration can be attributed mainly to magnetic interactions of larger size particles, besides non-magnetic interactions mediated by excess surfactant. The observed magnetoviscous effect is a consequence of the existing particle clusters in MF/OA, as detected by small angle scattering in the absence of the field.

This comprehensive comparative study of magnetic fluids with two different stabilization mechanisms – electrostatic and electro-steric – over a large concentration range, has thus identified both similarities and important differences on the microscopic and macroscopic level for these systems. SANS, SAXS, VSM, magnetogranulometry and magnetorheology, employed in this study, are practically the only techniques adequate to investigate concentrated magnetic fluids, without any modification of the original samples. The combination of these advanced techniques also with TEM, XPS and ATR-FTIR, as well as DLS, has been essential for elucidating the mechanisms in action, and we believe that the information obtained in this work can be beneficial for the optimization of magnetic fluids in different applications, such as some of those outlined in the introductory section of this work.

Conflicts of interest

There are no conflicts of interest to declare.

Acknowledgements

This work benefited by the support of the multi-annual Research Program (2016–2020) of the Lab. Magnetic Fluids (CFATR, Romanian Academy-Timisoara Branch). C. V. and R. T. acknowledge the financial support of the Romanian Authority for Scientific Research and Innovation, CNCS/CCCDI – UEFISCDI, project number PN-III-P2.2.1-PED-2016-0168, within PNCDI III. M. L. and R. H. A. R. were supported by the Academy of Finland Centres of Excellence Programme (2014–2019) and made use of the Aalto University Nanomicroscopy Centre premises. R. H. A. R. acknowledges also the support by the European Research Council ERC-2016-CoG (725513-SuperRepel). The authors are indebted to C. Leostean (INCDTIM Cluj-Napoca) for XPS and low temperature magnetization and to Oana Marinica (University Politehnica Timisoara) for room temperature VSM measurements. The active contribution of Florica Balanean (University Politehnica of Timisoara) in MF/water synthesis is highly appreciated. Valuable discussions in the framework of the COST Action TD1402 RADIOMAG are highly appreciated.

References

1 R. E. Rosensweig, *Ferrohydrodynamics*, Cambridge University Press, Cambridge, 1985, p. 344.
2 R. Massart, E. Dubois, V. Cabuil and E. Hasmonay, *J. Magn. Magn. Mater.*, 1995, **149**(1–2), 1–5.
3 V. Cabuil, J. C. Bacri, R. Perzynsky and Y. Raikher, in *Magnetic Fluids and Applications Handbook*, ed. B. M. Berkovski and V. G. Bashtovoy, Begell House, Washington, 1996, pp. 33–55.
4 S. Odenbach, in *Ferrofluids*, ed. K. H. J. Buschow, *Handbook of Magnetic Materials*, Elsevier Science, Amsterdam, 2006, vol. 16, pp. 127–208.
5 L. Vékás, M. V. Avdeev and D. Bica, in *NanoScience in Biomedicine*, ed. D. Shi, Springer, Berlin, Heidelberg, 2009, pp. 650–728.
6 R. Massart, in *Magnetic Fluids and Applications Handbook*, ed. B. M. Berkovski and V. G. Bashtovoy, Begell House, Washington, 1996, pp. 24–27.
7 R. Massart, *IEEE Trans. Magn.*, 1981, **17**(2), 1247–1248.
8 J. C. Bacri, R. Perzynski, D. Salin, V. Cabuil and R. Massart, *J. Magn. Magn. Mater.*, 1990, **85**(1–3), 27–32.
9 G. J. Fleer and J. Lyklema, in *Adsorption from solution at the solid/liquid interface*, ed. G. D. Parfitt and C. H. Rochester, Academic Press, London, 1983, pp. 153–220.
10 J. C. Bacri, R. Perzynski, V. Cabuil and R. Massart, *J. Colloid Interface Sci.*, 1989, **132**(1), 43–53.

11 F. Cousin, E. Dubois and V. Cabuil, *Phys. Rev. E: Stat., Nonlinear, Soft Matter Phys.*, 2003, **68**, 021405.
12 G. Mériguet, F. Cousin, E. Dubois, F. Boué, A. Cebers and B. Farago, *et al.*, *J. Phys. Chem. B*, 2006, **110**(9), 4378–4386.
13 E. Wandersman, E. Dubois, V. Dupuis, A. Duri, A. Robert and R. Perzynski, *J. Phys.: Condens. Matter*, 2008, **20**(20), 204124.
14 E. Wandersman, A. Cēbers, E. Dubois, G. Mériguet, A. Robert and R. Perzynski, *Soft Matter*, 2013, **9**(48), 11480.
15 E. Wandersman, Y. Chushkin, E. Dubois, V. Dupuis, A. Robert and R. Perzynski, *Soft Matter*, 2015, **11**(36), 7165–7170.
16 J. Shimoiizaka, M. Nakatsuka, T. Fujita and A. Kounosu, *IEEE Trans. Magn.*, 1980, **MAG-16**(2), 368–371.
17 S. Khalafalla and G. W. Reimers, *IEEE Trans. Magn.*, 1980, **MAG-16**(2), 178–183.
18 P. Tartaj, M. P. Morales, S. Veintemillas-Verdauger, T. Gonzales-Carreno and C. J. Serna, in *Handbook of Magnetic Materials*, ed. K. H. J. Buschow, Elsevier Science, Amsterdam, 2006. vol. 16, p. 403–82.
19 S. Laurent, D. Forge, M. Port, A. Roch, C. Robic and L. V. Elst, *et al.*, *Chem. Rev.*, 2010, **108**, 2064–2110.
20 K. M. Krishnan, *IEEE Trans. Magn.*, 2010, **46**, 2523–2558.
21 E. Amstad, M. Textor and E. Reimhult, *Nanoscale*, 2011, **3**(7), 2819–2843.
22 A. Wooding, M. Kilner and D. B. Lambrick, *J. Colloid Interface Sci.*, 1991, **144**(1), 236–242.
23 A. Wooding, M. Kilner and D. B. Lambrick, *J. Colloid Interface Sci.*, 1992, **149**(1), 98–104.
24 L. Shen, P. E. Laibinis and T. Hatton, *J. Magn. Magn. Mater.*, 1999, **194**(1), 37–44.
25 L. Shen, P. E. Laibinis and T. A. Hatton, *ACS Macro Lett.*, 1999, **15**(2), 447–453.
26 G. D. Moeser, K. A. Roach, W. H. Green, P. E. Laibinis and T. A. Hatton, *Ind. Eng. Chem. Res.*, 2002, **41**(19), 4739–4749.
27 R. Turcu, O. Pana, A. Nan, I. Craciunescu, O. Chauvet and C. Payen, *J. Phys. D: Appl. Phys.*, 2008, **41**(24), 245002.
28 D. Bica, L. Vékás, M. Avdeev, O. Marinică, V. Socoliuc and M. Bălăsoiu, *et al.*, *J. Magn. Magn. Mater.*, 2007, **311**, 17–21.
29 E. Tombácz, D. Bica, A. Hajdú, E. Illés, A. Majzik and L. Vékás, *J. Phys.: Condens. Matter*, 2008, **20**(20), 204103.
30 V. I. Petrenko, M. V. Avdeev, V. M. Garamus, L. A. Bulavin, V. L. Aksenov and L. Rosta, *Colloids Surf., A*, 2010, **369**(1–3), 160–164.
31 V. I. Petrenko, O. P. Artykulnyi, L. A. Bulavin, L. Almásy, V. M. Garamus and O. I. Ivankov, *et al.*, *Colloids Surf., A*, 2018, **541**, 222–226.
32 G a. Van Ewijk, G. J. Vroege and B. W. M. Kuipers, *Langmuir*, 2002, **18**(2), 382–390.
33 M. Balasoiu, M. V. Avdeev and V. L. Aksenov, *Crystallogr. Rep.*, 2007, **52**(3), 505–511.
34 E. Tombácz, I. Y. Toth, D. Nesztor, E. Illés, A. Hajdú and M. Szekeres, *et al.*, *Colloids Surf., A*, 2013, **435**, 91–96.
35 L. A. Harris, J. D. Goff, A. Y. Carmichael, J. S. Riffle, J. J. Harburn and T. G. St. Pierre, *et al.*, *Chem. Mater.*, 2003, **15**(2), 1367–1377.
36 N. Jain, Y. Wang, S. K. Jones, B. S. Hawkett and G. G. Warr, *Langmuir*, 2010, **26**(6), 4465–4472.
37 L. Shen, A. Stachowiak, S. E. K. Fateen, P. E. Laibinis and T. A. Hatton, *Langmuir*, 2001, **17**(2), 288–299.
38 J. C. Bacri, F. Boué, V. Cabuil and R. Perzynski, *Colloids Surf., A*, 1993, **80**(1), 11–18.
39 E. Dubois, V. Cabuil, F. Boue and R. Perzynski, *J. Chem. Phys.*, 1999, **111**, 7147–7160.
40 M. V. Avdeev, E. Dubois, G. Mériguet, E. Wandersman, V. M. Garamus and A. V. Feoktystov, *et al.*, *J. Appl. Crystallogr.*, 2009, **42**(6), 1009–1019.
41 M. V. Avdeev and V. L. Aksenov, *Phys.-Usp.*, 2011, **53**(10), 971–993.
42 D. Borin, A. Zubarev, D. Chirikov, R. Müller and S. Odenbach, *J. Magn. Magn. Mater.*, 2011, **323**(10), 1273–1277.
43 J. Nowak, F. Wiekhorst, L. Trahms and S. Odenbach, *J. Phys.: Condens. Matter*, 2014, **26**(17), 176004.
44 S. Roger, Y. Y. C. Sang, A. Bee, R. Perzynski, J. M. Di Meglio and A. Ponton, *Eur. Phys. J. E: Soft Matter Biol. Phys.*, 2015, **38**(8), 88.
45 J. Liu, C. Dai and Y. Hu, *Environ. Res.*, 2018, **161**, 49–60.
46 G. Béalle, R. Di Corato, J. Kolosnjaj-Tabi, V. Dupuis, O. Clément and F. Gazeau, *et al.*, *Langmuir*, 2012, **28**(32), 11834–11842.
47 C. Blanco-Andujar, D. Ortega, P. Southern, Q. A. Pankhurst and N. T. K. Thanh, *Nanoscale*, 2015, **7**(5), 1768–1775.
48 E. Tombácz, R. Turcu, V. Socoliuc and L. Vékás, *Biochem. Biophys. Res. Commun.*, 2015, **468**(3), 442–453.
49 R. Turcu, V. Socoliuc, I. Crăciunescu, A. Petran, A. Paulus and M. Franzreb, *et al.*, *Soft Matter*, 2015, **11**(5), 1008–1018.
50 W. Li, D. Liu, J. Wu, C. Kim and J. D. Fortner, *Environ. Sci. Technol.*, 2014, **48**(20), 11892–11900.
51 A. Jedlovszky-Hajdú, F. B. Bombelli, M. P. Monopoli, E. Tombácz and K. A. Dawson, *Langmuir*, 2012, **28**(42), 14983–14991.
52 T. Fujita, in *Magnetic Fluids and Applications Handbook*, ed. B. M. Berkovski and V. G. Bashtovoy, Begell House, Washington, 1996, pp. 755–789.
53 S. Odenbach, *Phys. Sep. Sci. Eng.*, 1998, **9**, 1–25.
54 J. Svoboda and T. Fujita, *Miner. Eng.*, 2003, **16**(9), 785–792.
55 J. Svoboda, *Magnetic techniques for the treatment of materials*, Kluwer Academic Publishers, Amsterdam, 2004, p. 642.
56 A. Walter, A. Garofalo, A. Parat, H. Martinez, D. Felder-Flesch and S. Begin-Colin, *Nanotechnol. Rev.*, 2015, **4**(6), 581–593.
57 Y. Sahoo, A. Goodarzi, M. T. Swihart, T. Y. Ohulchanskyy, N. Kaur and E. P. Furlani, *et al.*, *J. Phys. Chem. B*, 2005, **109**(9), 3879–3885.
58 J. V. I. Timonen, M. Latikka, O. Ikkala and R. H. A. Ras, *Nat. Commun.*, 2013, **4**, 1–8.
59 J. V. I. Timonen, M. Latikka, L. Leibler, R. H. A. Ras and O. Ikkala, *Science*, 2013, **341**, 253–257.
60 A. Hajdú, M. Szekeres, I. Y. Tóth, R. A. Bauer, J. Mihály and I. Zupkó, *et al.*, *Colloids Surf., B*, 2012, **94**, 242–249.
61 M. Szekeres, I. Tóth, E. Illés, A. Hajdú, I. Zupkó and K. Farkas, *et al.*, *Int. J. Mol. Sci.*, 2013, **14**(7), 14550–14574.
62 U.S. National Institutes of Health. ImageJ [Internet]. Bethesda, Maryland, USA, Rasband WS; 1997 [cited 2018 Jul 4], available from: https://imagej.nih.gov/ij/.

63 V. Socoliuc, V. Kuncser, R. Turcu and L. Vekas, in *New Developments in NMR No. 13 Contrast agents for MRI: experimental methods*, ed. V. C. Pierre and M. J. Allen, The Royal Society of Chemistry, Cambridge, 2018, pp. 387–422.
64 A. O. Ivanov, S. S. Kantorovich, E. N. Reznikov, C. Holm, A. F. Pshenichnikov and A. V. Lebedev, *et al.*, *Phys. Rev. E: Stat., Nonlinear, Soft Matter Phys.*, 2007, **75**(6), 061405.
65 D. Franke, A. G. Kikhney and D. I. Svergun, *Nucl. Instrum. Methods Phys. Res., Sect. A*, 2012, **689**, 52–59.
66 G. D. Wignall and F. S. Bates, *J. Appl. Crystallogr.*, 1987, **20**(1), 28–40.
67 M. Kotlarchyk and S. Chen, *J. Chem. Phys.*, 1983, **79**(5), 2461–2469.
68 D. J. Kinning and E. L. Thomas, *Macromolecules*, 1984, **17**(9), 1712–1718.
69 J. S. Pedersen, *Adv. Colloid Interface Sci.*, 1997, **70**, 171–210.
70 J. B. Hayter and J. Penfold, *Mol. Phys.*, 1981, **42**(1), 109–118.
71 J.-P. Hansen and J. B. Hayter, *Mol. Phys.*, 1982, **46**(3), 651–656.
72 H. M. Laun, G. Schmidt, C. Gabriel and C. Kieburg, *Rheol. Acta*, 2008, **47**(9), 1049–1059.
73 H. M. Laun, C. Gabriel and C. Kieburg, *J. Rheol.*, 2010, **54**(2), 327–354.
74 G. Cogoni, M. Grosso, R. Baratti and J. A. Romagnoli, *AIChE J.*, 2012, **58**(12), 3731–3739.
75 G. Cogoni, D. Widenski, M. Grosso, R. Baratti and J. A. Romagnoli, *Comput. Chem. Eng.*, 2014, **63**, 82–90.
76 I. J. Bruvera, P. Mendoza Zélis, M. Pilar Calatayud, G. F. Goya and F. H. Sánchez, *J. Appl. Phys.*, 2015, **118**(18), 184304.
77 R. Chantrell, J. Popplewell and S. Charles, *IEEE Trans. Magn.*, 1978, **MAG-14**(5), 975–977.
78 B. Luigjes, S. M. C. Woudenberg, R. de Groot, J. D. Meeldijk, H. M. Torres Galvis and K. P. de Jong, *et al.*, *J. Phys. Chem. C*, 2011, **115**(30), 14598–14605.
79 I. Y. Tóth, M. Szekeres, R. Turcu, S. Sáringer, E. Illés and D. Nesztor, *et al.*, *Langmuir*, 2014, **30**(51), 15451–15461.
80 D. Wilson and M. A. Langell, *Appl. Surf. Sci.*, 2014, **303**, 6–13.
81 S. Poulin, R. França, L. Moreau-Bélanger and E. Sacher, *J. Phys. Chem. C*, 2010, **114**(24), 10711–10718.
82 A. K. Gupta and M. Gupta, *Biomaterials*, 2005, **26**(18), 3995–4021.
83 M. Mahdavi, M. B. Ahmad, M. J. Haron, F. Namvar, B. Nadi and M. Z. A. Rahman, *et al.*, *Molecules*, 2013, **18**(7), 7533–7548.
84 E. Illés, M. Szekeres, E. Kupcsik, I. Y. Tóth, K. Farkas and A. Jedlovszky-Hajdú, *et al.*, *Colloids Surf., A*, 2014, **460**, 429–440.
85 H. Namduri and S. Nasrazadani, *Corros. Sci.*, 2008, **50**(9), 2493–2497.
86 M. Doucet, J. H. Cho, G. Alina, J. Bakker, W. Bouwman, P. Butler, *et al.*, *SasView version 4.1*, 2017 Mar 25 [cited 2018 Jul 4]; available from: https://zenodo.org/record/438138#.WzywSvZuLcs.

